1992

Eddy current inspection of weld defects in tubing

Gopichand Katragadda
Iowa State University

Eddy current inspection of weld defects in tubing

by

Gopichand Katragadda

A Thesis Submitted to the

Graduate Faculty in Partial Fulfillment of the

Requirements for the Degree of

MASTER OF SCIENCE

Department: Electrical Engineering and Computer Engineering
Major: Electrical Engineering

Iowa State University
Ames, Iowa

1992

TABLE OF CONTENTS

LIST OF SYMBOLS

$\overline{A}$	3D Magnetic vector potential	Weber/m
$\overline{\mathrm{A}}$	RMS phasor magnetic vector potential	Weber/m
$\overline{\mathbf{A}}$	Axisymmetric RMS phasor magnetic vector potential at any point	Weber/m
dc	direct current	
$\overline{D}$	Electric flux density	Coloumb/m^2
$\overline{E}$	Electric field intensity	Volt/m
$\overline{H}$	Magnetic field intensity	Ampere/m
$\overline{J}$	Current density	Ampere/m^2
σ	Electrical conductivity	mhos/m
μ	Magnetic permeability	Henry/m

ABSTRACT

Eddy current techniques using absolute probes find limited application to weld testing. Signals from the defects are masked in noise produced by lift-off, probe wobble and local changes in the permeability of the weld. Also, variations in the coil impedance caused by defects in the test specimen are often minuscule in comparison to the quiescent value of the coil impedance. These reasons led previous researchers to conclude that reliable detection or sizing of weld defects was difficult using Eddy current methods.

Differential probes overcome these shortcomings. They are being used increasingly in flaw detection and are ideal for testing tube geometries. In this thesis, an approach using differential probes for inspection of weld defects in small diameter tubing is described. A finite element code is used to model the weld region and defects. The validity of this code is assumed, as proven by previous research, and parameters in the 'weld region model' are changed to obtain numerical results that match experimental results. Simple defects are simulated in the 'weld region model' developed and compared with experimental results to cross check the validity of the code. The comparison of numerical and experimental results is also used to study weld region conductivity. An approach to overcome the problem of permeability variations in the case of ferromagnetic tube inspection is described.

Impedance plane signals are predicted for different weld defect types and compared wherever possible with signals from actual welds in tubing. It is shown that it is possible to differentiate between weld region signals and signals obtained from other flaws. Also, it is shown that it is possible to differentiate between defective welds and good welds. For a weldment between tubes of the same material, produced in different batches, a unique impedance plane trajectory is traced. This phenomenon is due to the small difference in conductivity between tubes produced in different batches. This is a very important result since impedance plane trajectories from welds could be very easily isolated from other defect signals. In summary, this study shows that the differential probe eddy current method has good potential in tube weld testing. This study also shows the validity and simplicity of the axisymmetric finite element code for modeling field/material interaction.

ACKNOWLEDGMENTS

"A complete engineer is one who has efficiently combined the complementary aspects of theoretical studies and industrial applications in his work". This view of Dr. William Lord, my major advisor, has been the driving force behind the successful completion of the NASA-funded space shuttle main engine heat exchanger tubing inspection project of which this research is part. I am deeply indebted to Dr. Lord for his guidance and encouragement throughout the course of this project. I also thank him for the number of hours he put into proof reading this thesis, suggesting several vital changes, which were responsible for this thesis maturing from its infancy to its present form.

I thank Dr. Lalita Udpa for her interest in this work and her help and ideas especially in the defect classification aspect of this project, which is an outgrowth of an earlier work done by her and Dr. Satish Udpa. Dr. Hsung Chen Hsieh and Dr. Vinay Dayal have constantly encouraged me and have shown deep interest in this work which gave me added zeal for this research. I thank them for consenting to be on my committee.

I thank my colleagues Shridhar Nath and Steven Ross for their help and support. I thank my fellow students at the electrical engineering department for their help and encouragement.

Lastly, I thank NASA whose funding made this project possible.

1 OVERVIEW

1.1 Introduction

A nondestructive test can be described [1] as being an examination of an object in any manner which will not impair the future usefulness of the object. The purpose of the examination may be to detect internal or external flaws, to measure thickness, to determine material structure or composition, or to measure or detect any of the properties of the object. The test may be a simple visual one, or it may involve some form of electromagnetic energy including visible light, X-rays, infrared rays, microwaves and alternating or direct current. The test may involve vibrational energy (sound) over a wide range of frequencies (ultrasonics).

In general, a nondestructive testing (NDT) procedure includes (Fig. 1.1):

1. An energy source or excitation signal.
2. The input transducer which couples excitation energy to the specimen.
3. The energy defect interaction.
4. The output transducer which senses the energy defect interaction.
5. The signal from the output transducer which is displayed in a format useful for analysis and interpretation.
6. The signal interpretation.

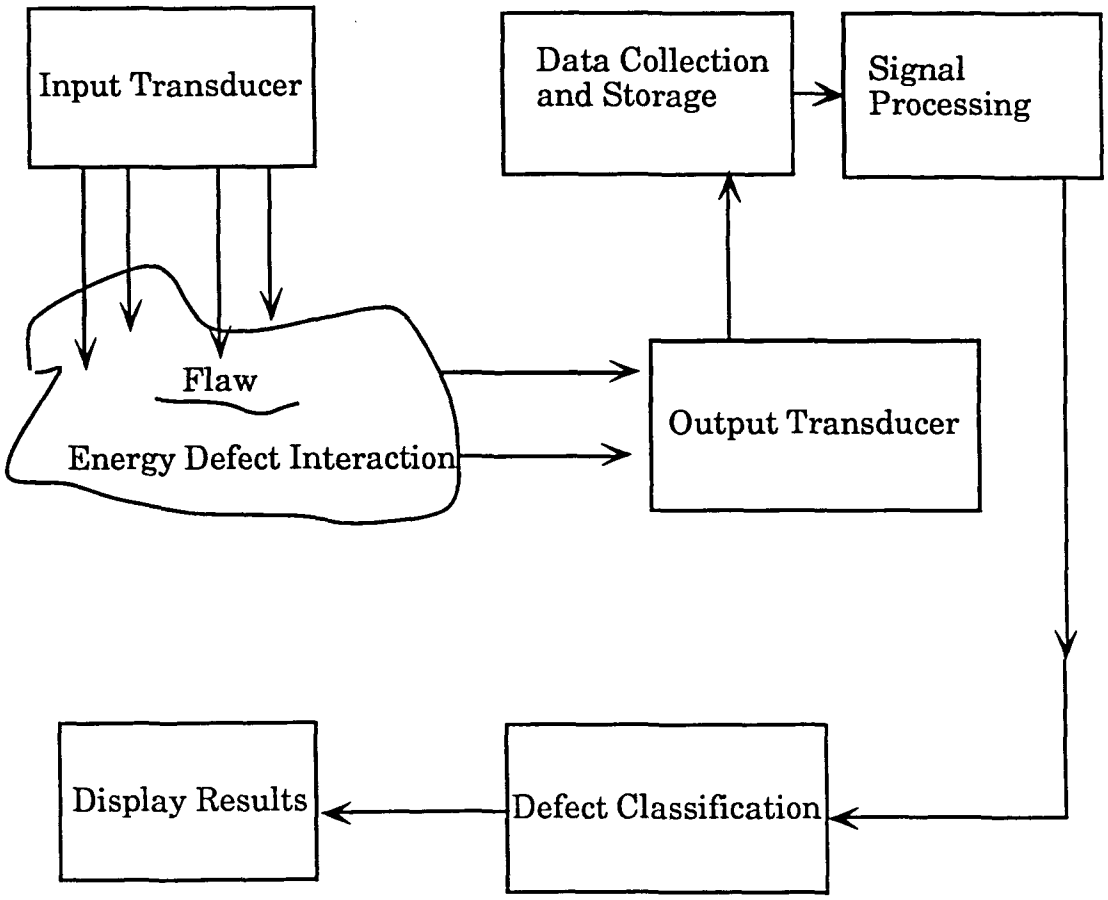

Fig. 1.1. Generalized NDT procedure

Nondestructive tests are an essential component of the production process. These tests have come to be accepted as more sensitive, accurate and reliable than 'destructive tests' such as fatigue testing, mechanical gauging or hardness testing. Disaster and loss of life or of high investments in complex engineering developments can result from omission of necessary tests on components in fields such as commercial aircraft, missiles, space vehicles and nuclear systems.

In this thesis, a description of an electromagnetic nondestructive testing (NDT) method (eddy current technique) for the inspection of small diameter tubing is given. Specifically, this work is part of a NASA-funded project which involves the building of a complete eddy current test system for space shuttle main engine (SSME) heat exchanger tubing inspection (Fig. 1.2). It should be pointed out that the heat exchanger tubing has never failed before. However, there have been cases where weld regions of the heat exchanger tubing have failed quality inspection tests [2]. This work is an effort in making early detection and classification of weld defects accurate and simple.

An overview of the heat exchanger tubing inspection project is given in Fig. 1.3. Other than weld signals and weld defect signals, the tight crack signals [3] and support plate signals [4] are also studied. Impedance plane trajectories (IPT) traced due to welds or other defects are digitized and stored on a computer. The IPT's can be viewed on the eddyscope or viewed at a later time on the computer. Features are extracted from the raw signal data for purposes of data compression and incorporation into a learning algorithm. The learning algorithm is used to discriminate between welds and other defect signals and also between good welds and defective welds. Depending on the type of features extracted, reconstruction and plotting is possible from the features.

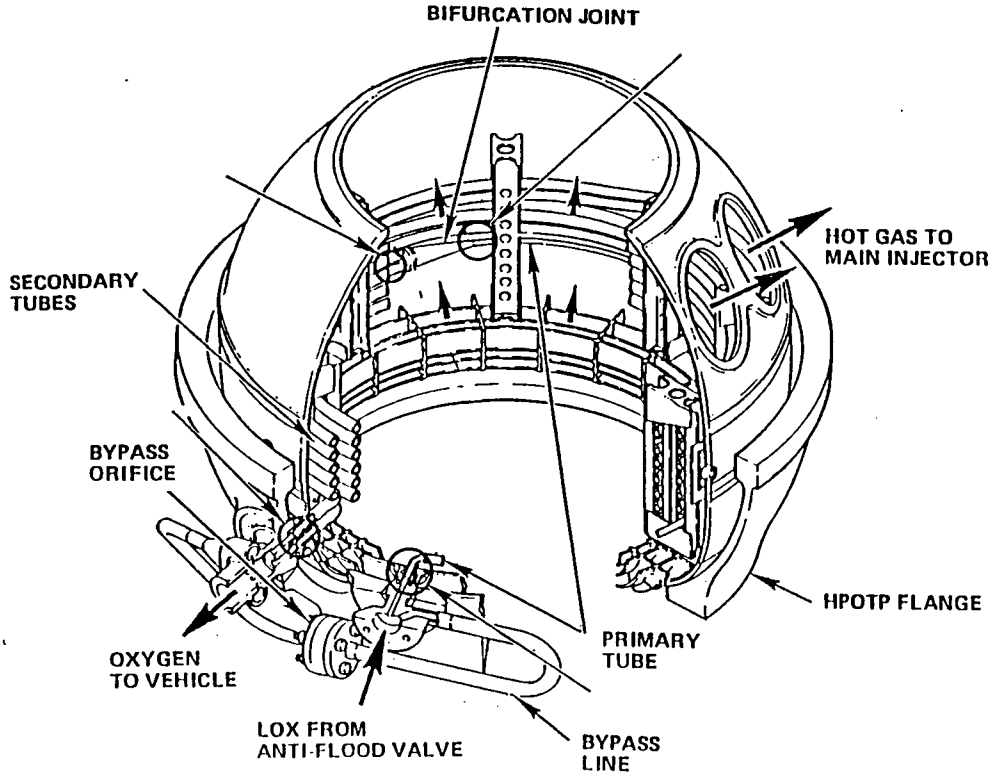

Fig. 1.2 Space shuttle main engine heat exchanger tubing

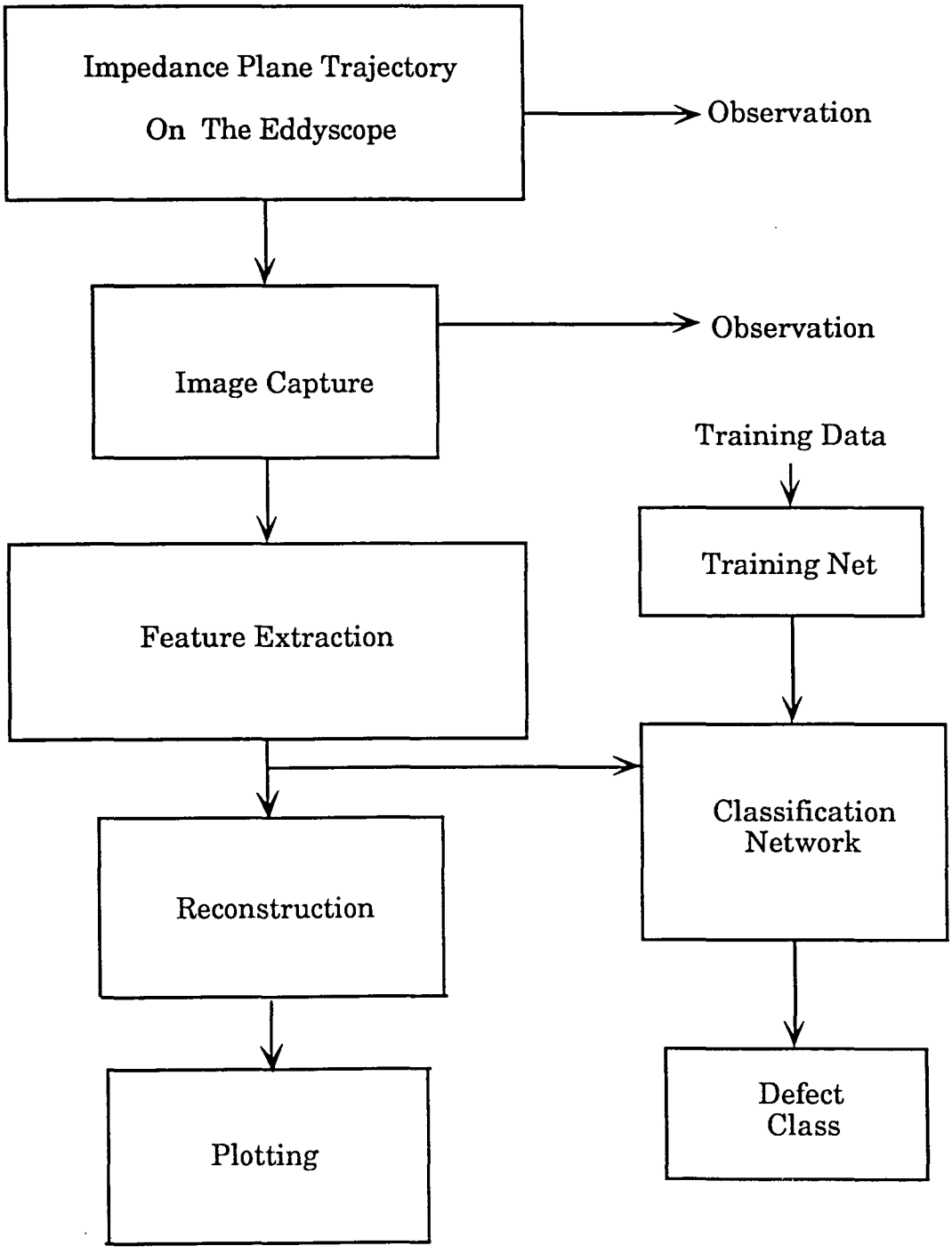

Fig. 1.3 An overview of the project

1.2 Types of NDT

NDT techniques can be classified based on the governing partial differential equation (PDE). NDT techniques can also be characterized by the excitation or the energy source frequency. A brief discussion of the important NDT methods for weld quality assurance is given in the following paragraphs.

1.2.1 Detection of surface flaws

Surface breaking flaws are more detrimental to weld integrity than embedded flaws of the same size, so their detection and removal is essential [5]. Welding imperfections such as undercuts can be detected by visual inspection; this important NDT method should not be underestimated. Smaller flaws not visible to the naked eye can be examined by increasing the contrast between the flaw and the parent material. This can be done by magnetic particle inspection or the dye penetrant method. Eddy current testing mainly finds application in detecting surface flaws in welds, though in this study, the differential probe eddy current method has been shown to detect subsurface flaws in tubing.

1.2.2 Detection of internal flaws

Critical weld joints need to be subjected to an inspection for internal flaws [5]. Two well established methods for detection of internal flaws are

radiography and ultrasonic testing. Radiography is the older-established technique, used since 1917 [5]; ultrasonic testing was introduced much later in 1942 [5]. Radiography produces an image of the lateral extent of the flaws on photographic film that can be scrutinized. Ultrasonic techniques produce echo signals on a CRT display which have to be converted into a geometric plot of flaws by the technician.

A detailed discussion of the different defects of importance in tube welding is given in Chapter 2. A discussion of electromagnetic NDT methods is given in the next section.

1.3 Electromagnetic NDT

Electromagnetic field interactions with metals can be used to determine both material properties and the presence of defects [6,7]. Such techniques are used widely in the testing of critical components for aerospace, transportation, energy and metal industries where quality assurance and reliability are a priority. Traditional electromagnetic NDT methods cover a wide range of frequencies from dc to microwave. However, common industrial techniques for metal inspection are limited to active dc, residual and eddy current forms of excitation; all low frequency phenomena for which displacement current effects can be neglected.

Those electromagnetic nondestructive testing techniques characterized as requiring a continuous dc source of excitation are classified as 'active' methods.

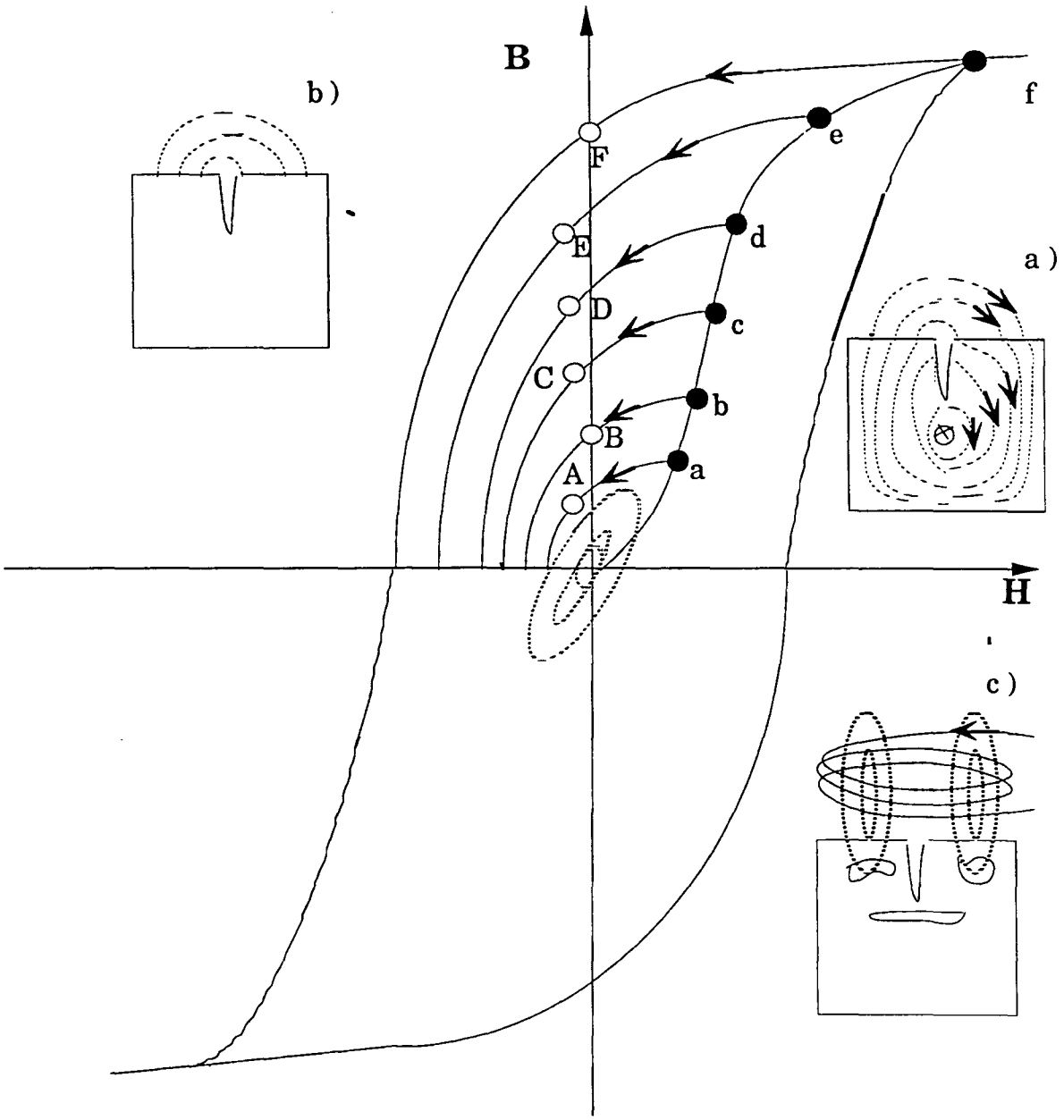

Fig. 1.4 Hysterisis curve and the three types of electromagnetic NDT [6]

a) Active leakage field b) Residual leakage field c) Eddy Current

Important amongst these methods are magnetic particle testing, magnetography, perturbation techniques, the potential drop method and

the variable reluctance probe method. In these methods (other than the potential drop method) an active leakage field is set up around the defect, which can be measured by flux density sensitive transducers. Ferromagnetic materials operating under this excitation mode are characterized by the initial portion of the magnetization curve between points 'a' - 'e' shown in Fig. 1.4 [6]. Residual leakage fields exist around defects in ferromagnetic specimens after the active dc excitation current is removed. Methods involving the measurement of these residual fields are classified as residual leakage field methods [6]. Portion 'A' - 'E' on the hysterisis curve (Fig. 1.4) represents the characteristic behavior of materials subject to residual excitation.

Eddy current techniques involve alternating current. Here both ferromagnetic and non ferromagnetic materials can be tested non destructively. The presence of defects or other inhomogenities cause induced eddy current paths and magnetic fields to change (Fig. 1.5), resulting in measurable variations in the test coil impedance.

The differential probe eddy current technique used in this work is described in detail in Chapter 3.

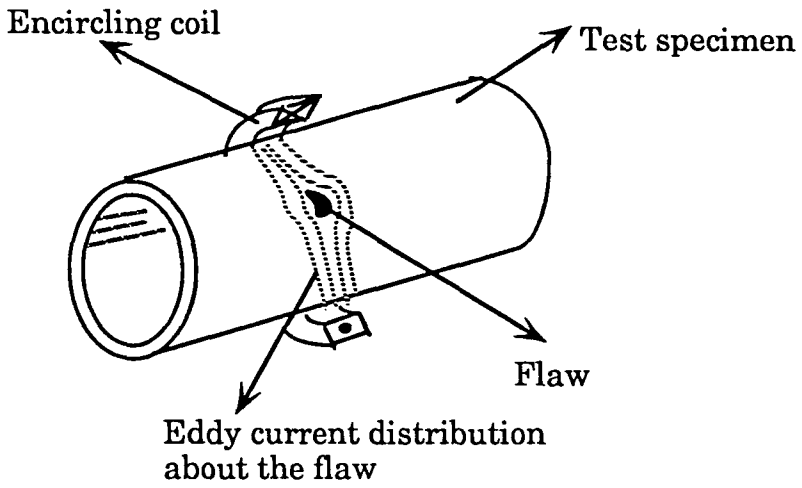

Fig. 1.5 Eddy current distribution modification due to presence of a defect [6]

1.4 Numerical Modeling

Numerical analysis techniques, primarily finite difference and finite element methods, have been used for some time to study dc and low frequency electromagnetic fields [8,9,10]. A number of advantages have been shown to favor the finite element approach for such studies, including ease of handling boundary conditions, ability to follow awkward boundary shapes, and relative economy of computer facilities usage. These factors are of utmost importance in electromagnetic nondestructive testing, and hence good progress has been made in applying the numerical techniques to model eddy current and active and residual leakage field NDT phenomena.

Such models are important in visualizing the physics of the field-defect interaction, designing test rigs and probes, developing training data

for automated defect characterization schemes, and simulating those test situations difficult to replicate in the laboratory.

Chapter 4 discusses the finite element axisymmetric code used in this work.

1.5 Feature Extraction and Defect Classification

One way of obtaining information regarding sizing and the type of defect from an impedance plane trajectory, is an experienced operator interpreting the signal by visual inspection. However an automated system, which is an optimal solution between computer interpretation and operator interpretation is more accurate and dependable. Chapter 5 describes a method in which features are extracted from the raw signal data and are incorporated into a training algorithm for classification purposes.

Chapter 6 discusses the test system developed for experimental measurements and computation in this study.

2 TUBING WELD DEFECTS

2.1 Introduction

Welding is a complicated process involving a number of variables which cannot be totally controlled in exactly the desired manner. This means that in spite of extreme care taken in the selection of materials and in the welding process, welded structures produced at an economic cost may contain a proportion of weld defects. In order to define a safe, realistic tolerance limit for each class of welds we first need to know the significance of different welds in terms of weld performance. What follows is a discussion of some of the common weld defects in tubing. All the pictures in this chapter are reproduced from an EPRI Special Report (Sept. 1980) 'NDE Characteristics of Pipe Weld Defects'. This reproduction is authorized by EPRI. The specimens are circumferential butt welds in Type 304 stainless steel. The weld defects shown were deliberately induced.

2.2 Cracks

Cracks are linear ruptures in the material. They can result from various causes, but all are essentially a function of microstructure and stress. In the heat exchanger tubing, cracks in welds could occur and grow during the flight of the space shuttle. Hence early detection of cracks is essential. Fig. 2.1 shows a photomacrograph (magnified photograph) of a crack.

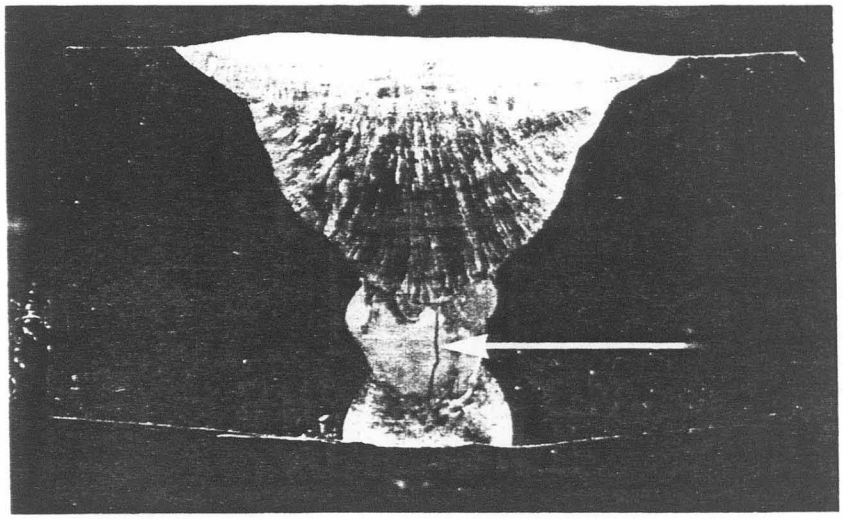

Fig. 2.1 Photomacrograph of a crack

2.3 Incomplete Fusion

Incomplete fusion is the failure of the parent material and the weld material to fuse together. This could result from insufficient weld current, too fast a welding speed or the presence of slag, oxides or other foreign material. Fig. 2.2 shows a photomacrograph of an incomplete fusion situation.

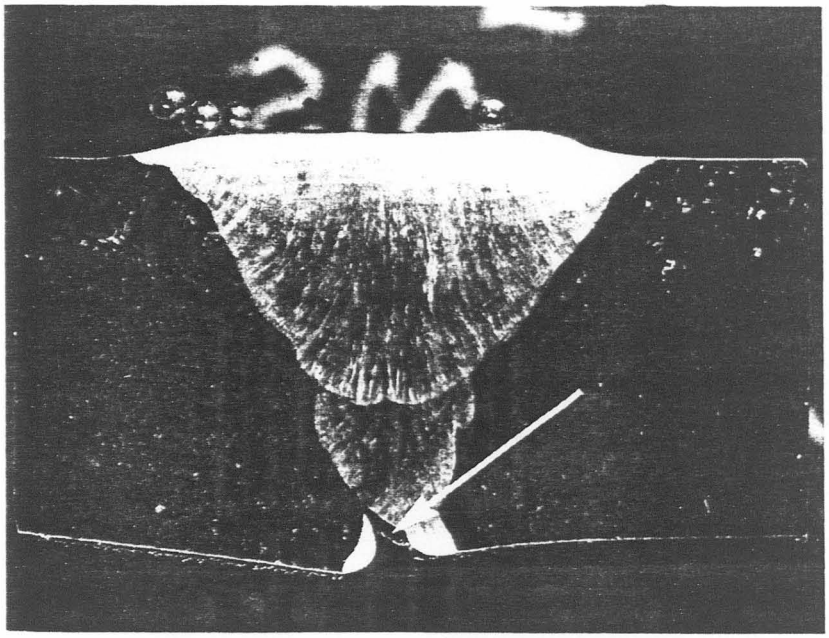

Fig. 2.2 Photomacrograph of incomplete fusion at the root

2.4 Incomplete Penetration

Incomplete penetration is the condition where the weld material fails to penetrate and fuse to the desired depth in the parent material. This could result from not providing enough root gap during the fitup operation, or the root gap closing due to residual welding stresses. Fig. 2.3 shows a photomacrograph of an incomplete penetration situation.

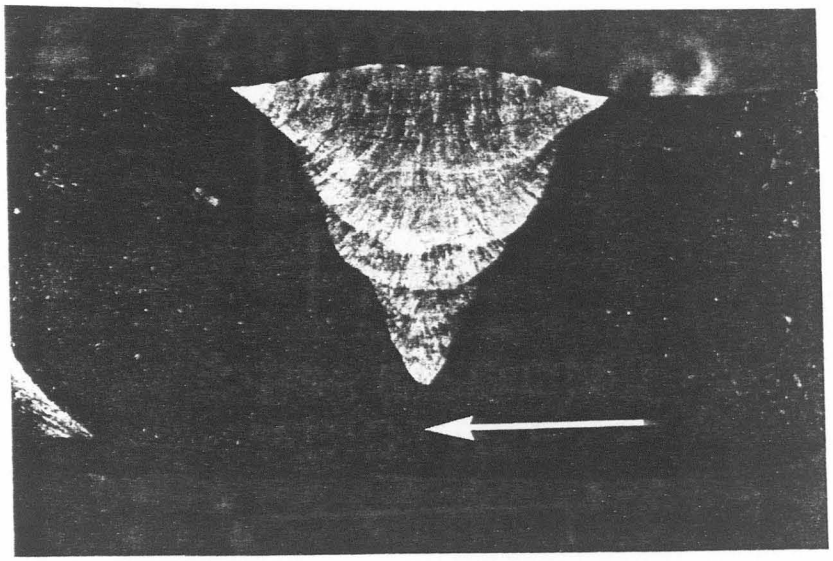

Fig. 2.3 Photomacrograph of inadequate penetration

2.5 Mismatch

Mismatch can be defined as the centerline offset in portions of the tube on either side of the weld. This is a result of poor workmanship or sometimes due to slight differences in the thickness of the two members in a butt weld. Fig. 2.4 shows a photomacrograph of a mismatch defect.

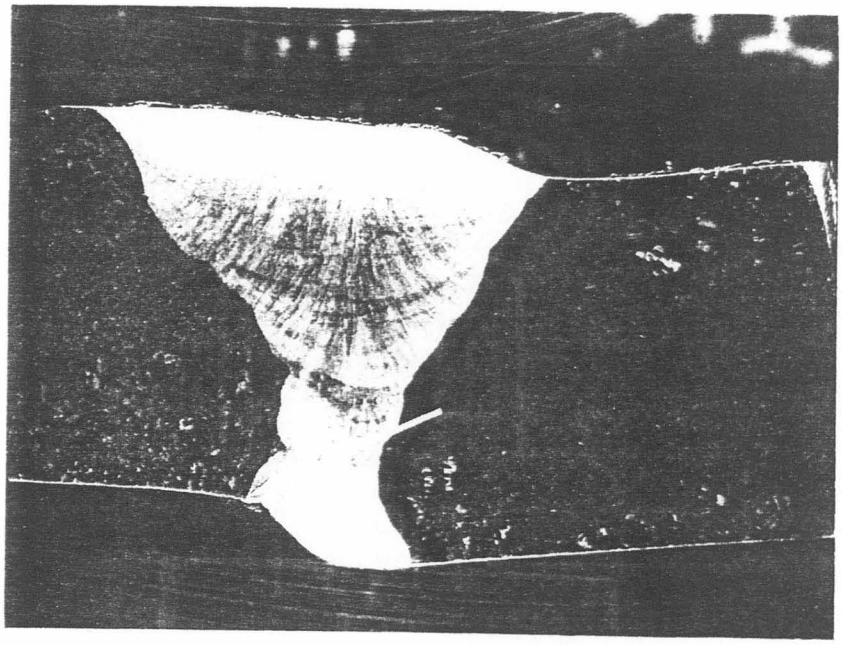

Fig. 2.4 Photomacrograph of a mismatch

2.6 Porosity

Porosity is the presence of globular voids in the weld material. These voids could result from gases released from the cooling weld material or from gases released due to chemical reactions in the weld. Fig. 2.5 shows a photomacrograph of porosity in a weld.

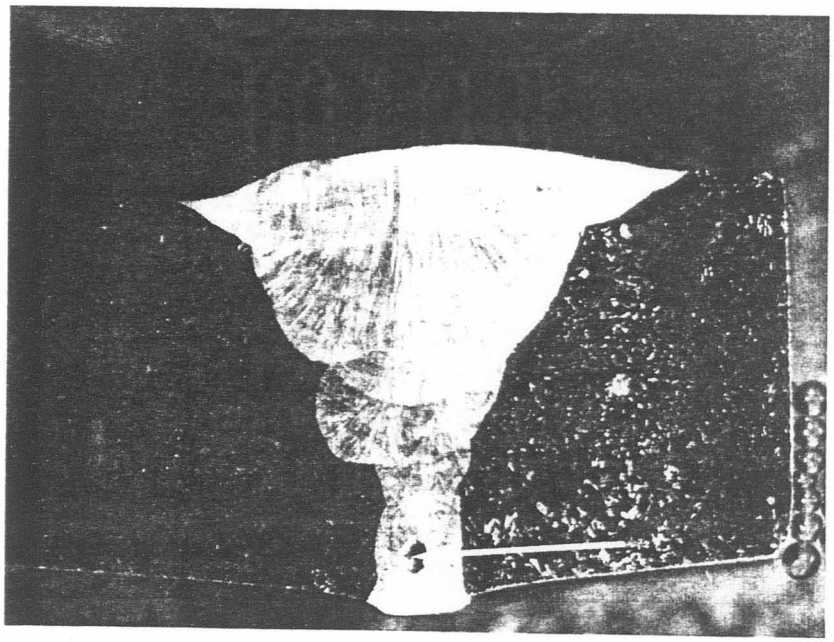

Fig. 2.5 Photomacrograph of porosity

2.7 Slag

Slag inclusions are oxides and other nonmetallic solid materials that get trapped in the weld material or between the weld material and the parent material. They are generally created by the molten fluxes employed in welding operations. Fig. 2.6 shows a photomacrograph of slag inclusion in a weld.

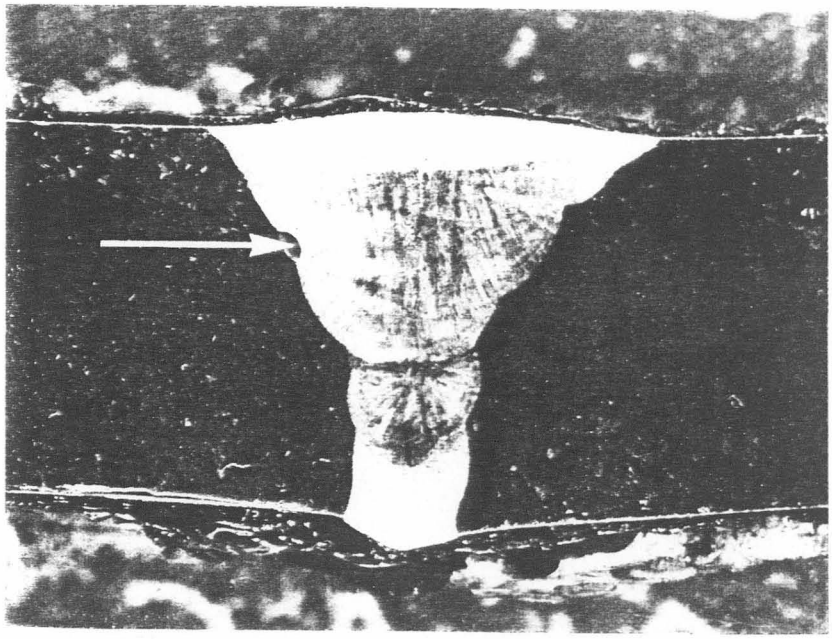

Fig. 2.6 Photomacrograph of slag inclusion

2.8 Undercut

Undercut is a serious defect which results from using improper welding techniques. The defect is a groove along the edge of the parent material and the weld material, left unfilled by the parent material. Fig. 2.7 shows a photomacrograph of an undercut.

It is of course desirable that welds be produced without any defects. However, practically there will always be a proportion of defective welds in any welding process. Hence improved techniques of inspection should be adopted for reliable detection of weld defects. Chapter 3 discusses the eddy current method and its possible use in the detection and sizing of weld defects.

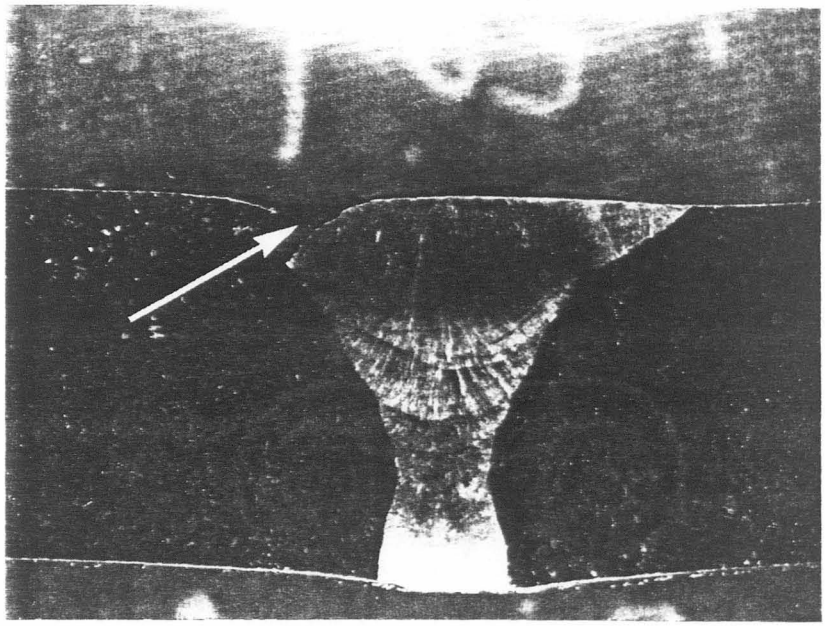

Fig. 2.7 Photomacrograph of an undercut on the outside diameter

3 EDDY CURRENT INSPECTION OF WELDMENTS

3.1 Introduction

Weld quality is a relative term which depends on the final use of the weldment. Some defects of importance studied in this work include (also refer Chapter 2):

1. Porosity: Globular voids free of any solid material resulting from chemical reactions taking place during welding.
2. Nonmetallic inclusions: Globular inclusions of nonmetallic solids that may have been produced during the welding process.
3. Cracking: Results from presence of multidirectional, localized stresses that at some point exceed the ultimate strength of the material.
4. Incomplete penetration: Failure of deposited metal and base metal to fuse integrally at the root.

The principal nondestructive testing methods for weldments are visual, radiographic, magnetic-particle, liquid penetrant and ultrasonic methods. In this study an evaluation is made of the differential probe eddy current testing of weld regions in tubing.

Nondestructive testing (NDT) enables aspects of weld quality to be revealed which cannot be observed by the naked eye. NDT can be used in the general assessment of material properties, for example for material sorting or for checking whether or not metals have been heat treated, but the most widespread use of NDT for welded fabrications is to assess weld imperfections. The extent to which NDT is applied depends on economy /

criticality tradeoffs. However, NDT must be included as part of the fabrication process in order to maintain product quality and minimize disruption to production.

The eddy current method is generally used to detect surface or near surface flaws in conducting material. This method is not often used for testing welded joints because of the many variables that can affect the result. However, the method is used for inspection of weldments in tubes and good results have been claimed for in-service inspection of offshore structures [11].

3.2 Principles of Eddy Current Testing

In eddy current inspection the alternating magnetic field of a coil carrying an alternating current produces eddy currents in the specimen under inspection. This results in an induced alternating field in the vicinity of the specimen. The induced field, which is in a direction opposing the primary field of the coil in accordance with Lenz's law, superimposes on the primary field. The net result is that the magnetic field near the coil is modified in the presence of a test object. The corresponding changes in impedance of the coil are measured as the total amplitude or by separating the real and imaginary components. This change in impedance is different in the case of a defect being present because of the disturbance to the eddy current distribution and its associated magnetic fields caused by the presence of a defect (Fig. 1.5).

In practice, the impedance of the test coil is not only modified by the defects but also by other disturbing parameters. The most important of these are [12]:

1. Lift-off variations - the variation of spacing between coil and specimen.
2. Local variations of magnetic permeability and electric conductivity resulting from the welding process. The most inhomogenous regions with regard to permeability and conductivity are the heat affected zones in the parent material on either side of the weld interface.
3. Bridging - existence of metallic contact along crack faces which can be particularly pronounced if the crack is under compressive stress.

3.3 The Farrowtest

At this stage it is appropriate to describe the Farrowtest [13], an eddy current test method which has been used for more than 45 years now, to test thousands of miles of tubing.

Fig. 3.1 shows a typical Farrowtest coil assembly. The Farrowtest operates by inducing alternating eddy current flow in the pipe wall. Detection of defects is accomplished by passing the pipe through the coil assembly. Defects interrupt and change the path of induced currents and the detector coils pick up these changes. The magnitude of the change is proportional to the size of the defect. The function of the dc coil is to induce magnetic saturation in the material under test. Magnetic saturation results in a relative permeability of 1.0 (or very close to 1.0). This is done for two reasons; one, to increase the depth of eddy current penetration and the

other, to overcome the problems of permeability changes in the case of ferromagnetic tubing. Both these aspects are discussed in more detail in sections 2.6 and 2.7 respectively.

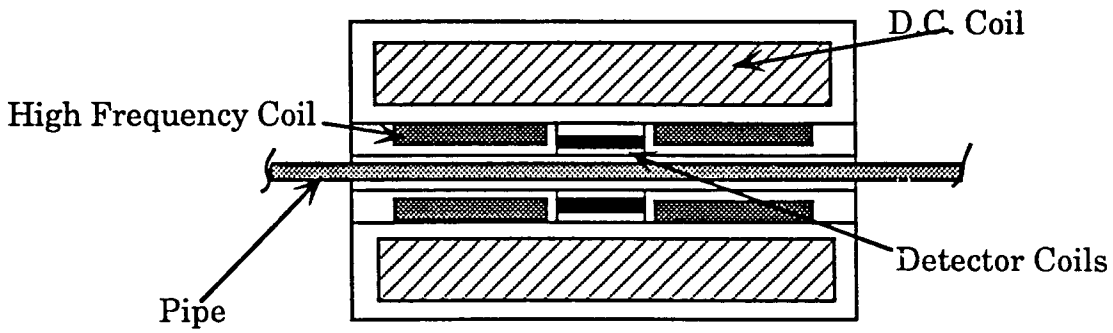

Fig. 3.1 The Farrowtest assembly

3.4 Principles of Differential Probe Testing

Differential eddy current probes overcome some of the difficulties mentioned in the previous section. A differential eddy current probe is shown in Fig. 3.2. The probe consists of two identical coils mounted on the same axis as the tube but spaced a small distance apart. The two coils form the two arms of a bridge circuit, which is initially nulled when the probe is stationed in a defect free segment of the tube. The balance is upset when either the leading or the trailing coil comes under a defect. The imbalance signal which is linked to the difference between the impedance of the two coils traces out a trajectory as shown in Fig. 3.3 for an

axisymmetric defect. The imbalance signal is traced out in opposite directions for the cases of leading and trailing edges of the coil under the defect, accounting for the two lobes in the impedance plane trajectory (IPT). When both the coils are far from the defect or when both are equally spaced under the defect the probe impedance is constant at the origin.

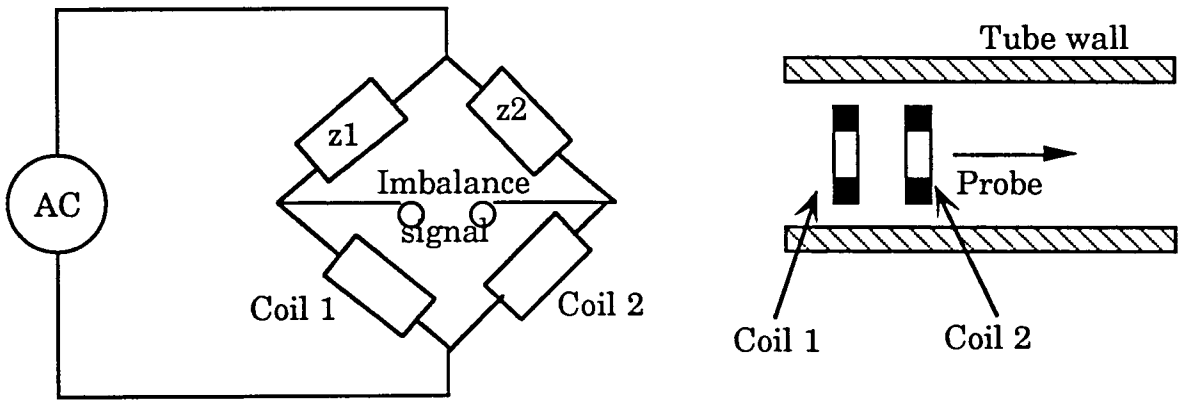

Fig. 3.2 Construction of the eddy current differential probe

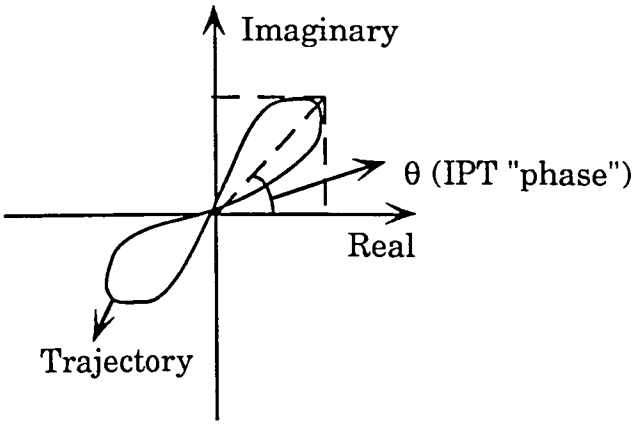

Fig. 3.3 A typical impedance plane trajectory

The differential nature of the probe makes the arrangement insensitive to environmental effects. In addition the differential connection results in the cancellation of the quiescent value of the coil impedance thereby highlighting the variations due to defects rather than the absolute value of the impedance.

3.5 Governing Equations

The governing partial differential equation for eddy current phenomena is derived from Maxwell's equations:

$$\nabla \times \overline{E} = -\frac{\partial \overline{B}}{\partial t} \qquad \text{(Maxwell-Faraday Law)} \qquad (3.1)$$

$$\nabla \times \overline{H} = \overline{J} + \frac{\partial \overline{D}}{\partial t} \qquad \text{(Maxwell-Ampere Law)} \qquad (3.2)$$

$$\nabla \cdot \overline{B} = 0 \qquad (3.3)$$

$$\nabla \cdot \overline{D} = \rho \qquad \text{(Gauss' Law)} \qquad (3.4)$$

Since $\nabla \cdot \overline{B} = 0$, we can express $\overline{B}$ (using the definition of magnetic vector potential) as [1]:

$$\overline{B} = \nabla \times \overline{A} \qquad (3.5)$$

Using equation 3.5 in equation 3.1;

$$\nabla \times \overline{E} = -\nabla \times \frac{\partial \overline{A}}{\partial t} \tag{3.6}$$

that is,

$$\nabla \times \left(\overline{E} + \frac{\partial \overline{A}}{\partial t} \right) = 0 \tag{3.7}$$

From the definition of electric potential Φ:

$$\overline{E} + \frac{\partial \overline{A}}{\partial t} = -\nabla \Phi \tag{3.8}$$

For an isotropic conducting medium:

$$\overline{J} = \sigma \overline{E} \tag{3.9}$$

Using equation 3.9 in equation 3.8:

$$\overline{J} = -\left(\sigma \frac{\partial \overline{A}}{\partial t} + \sigma \nabla \Phi \right) \tag{3.10}$$

substituting for $-\sigma \nabla \Phi$ as $\overline{J}_s$, the source current density:

$$\overline{J} = -\sigma\frac{\partial \overline{A}}{\partial t} + \overline{J}_s \qquad (3.11)$$

For the quasi-static case of eddy current phenomena the displacement current term in equation 3.2 can be neglected since at the relative low frequencies of operation the displacement current density is very less compared to the conduction current density [1]. Hence,

$$\nabla \times \overline{H} = \overline{J} \qquad (3.12)$$

Using equation 3.12 in equation 3.11,

$$(\nabla \times \frac{1}{\mu}\overline{B}) = \overline{J}_s - \sigma\frac{\partial \overline{A}}{\partial t} \qquad (3.13)$$

Substituting for $\overline{B}$ from equation 3.15:

$$(\nabla \times (\frac{1}{\mu}(\nabla \times \overline{A}))) = \overline{J}_s - \sigma\frac{\partial \overline{A}}{\partial t} \qquad (3.14)$$

We have the vector identity:

$$\nabla \times (\nabla \times \overline{A}) = \nabla . (\nabla . \overline{A}) - \nabla^2 \overline{A} \qquad (3.15)$$

and the Coulomb gauge

$$\nabla . \overline{A} = 0 \qquad (3.16)$$

Using equation 3.16 and equation 3.15 in equation 3.14 and assuming a homogenous, isotropic medium:

$$\frac{1}{\mu}(\nabla^2 \overline{A}) = \sigma \frac{\partial \overline{A}}{\partial t} - \overline{J}_s \qquad (3.17)$$

Assuming steady state harmonic fields [1] equation 3.17 can be written as:

$$\frac{1}{\mu}(\nabla^2 \overline{A}) = j\omega\sigma \overline{A} - \overline{J}_s \qquad (3.18)$$

which for the two-dimensional case reduces to

$$\frac{1}{\mu}\left(\frac{\partial^2 \overline{A}}{\partial x^2} + \frac{\partial^2 \overline{A}}{\partial y^2}\right) = j\omega\sigma \overline{A} - \overline{J}_s \qquad (3.19)$$

and for the axisymmetric case,

$$\frac{1}{\mu}\left(\frac{\partial^2 \overline{A}}{\partial r^2} + \frac{1}{r}\frac{\partial \overline{A}}{\partial r} + \frac{\partial^2 \overline{A}}{\partial z^2} - \frac{\overline{A}}{r^2}\right) = j\omega\sigma \overline{A} - \overline{J}_s \qquad (3.20)$$

Equation 3.20 uses the cylindrical coordinate system (r, ϕ, z) and is based on the assumption that the magnetic vector potential has a component in the ϕ direction only [1]. For the case of differential probe tube testing, equation

3.20 is the governing equation. A finite element approach to solving the governing equation is described in Chapter 4.

3.6 Skin Depth Considerations

The depth at which a defect can be detected is dependent on the depth to which the magnetic fields penetrate. The 'skin depth' or the 'standard depth of penetration' which gives an effective measure of the depth of penetration is defined as: 'The depth at which the amplitude of the magnetic field falls to 100/e percent of the field at the surface of the specimen' [1]. The equation for skin depth is derived starting from Maxwell's equations and making the following assumptions:

1. The conducting medium is linear, homogenous and isotropic.
2. The fields are steady state harmonic fields.

The equation obtained is [1]:

$$\delta = \left(\frac{1}{\pi f \mu \sigma}\right)^{1/2} \qquad (3.21)$$

The skin depth hence is a function of conductivity, permeability, and the frequency of operation. The conductivity is fixed but the frequency and permeability (in the case of ferromagnetic materials) can be altered by magnetizing the material under test, to obtain the desired skin depth. It should be pointed out that this classical definition of skin depth holds exactly only for an infinite half space. There is a deviation from this standard skin depth in any other situation. Hence this definition of skin

depth can only give us an approximate estimate of the true skin effect in more complex geometries [33].

3.7 Testing of Ferromagnetic Tube Welds

The main problem in the inspection of ferromagnetic tubes is that of permeability variations. Permeability variations result in the defect signals having an extremely poor signal-to-noise ratio. There are two aspects of permeability changes to be dealt with, one of which is the permeability change all along the length of the tube caused by localized stress over the surface of the tubing. The other is the local permeability variation in the weld region due to the heat effects.

One of the most successful methods of eliminating the effect of permeability variations is to apply a magnetic biasing field to reduce incremental permeability to a negligible level [14]. Fig. 3.4 shows two hysterisis loops that represent the extreme limits of difference in magnetic characteristics. It is seen that near saturation the incremental permeability defined by $\Delta B/\Delta H$ is essentially the same. Hence, eddy current testing can be carried out by using the technique of magnetic saturation to counter the effects of permeability changes. The saturating equipment is usually a solenoid coil carrying sufficient direct current to magnetically saturate the pipe within the coil.

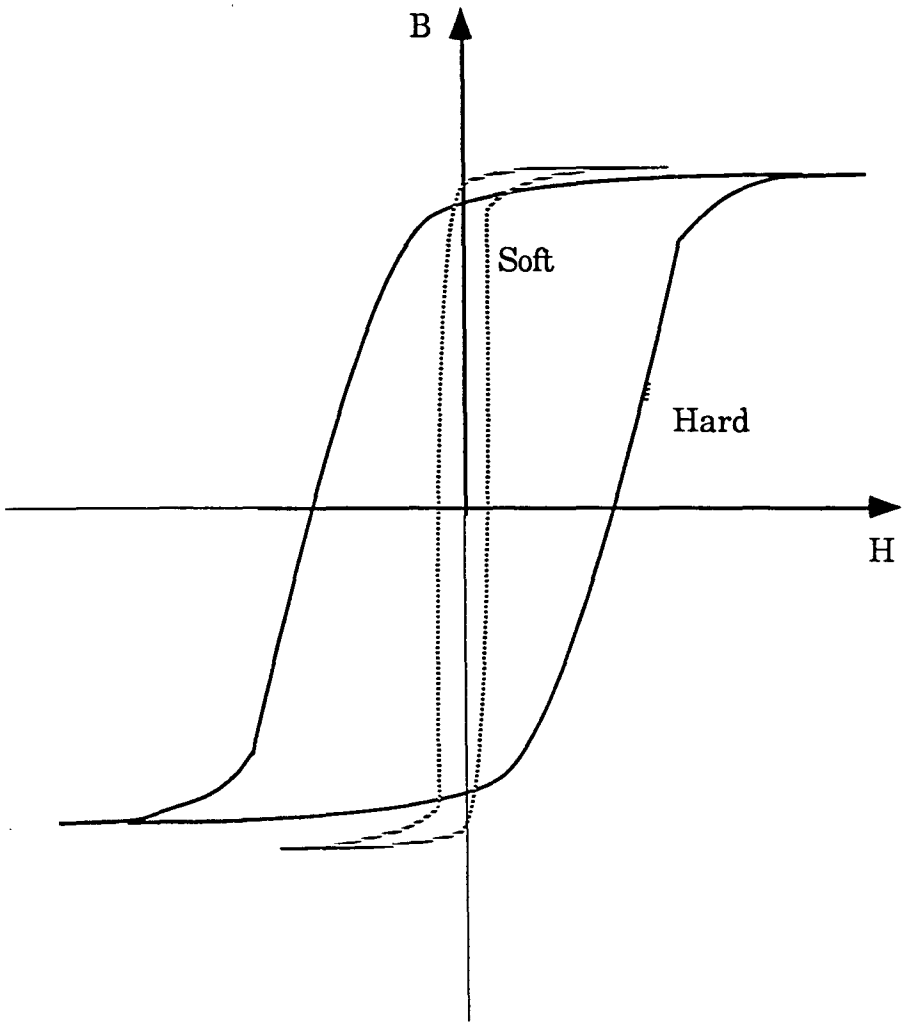

Fig. 3.4 Hysterisis loops for soft and hard material

4 FINITE ELEMENT MODELING

4.1 Introduction

Analytic solutions of partial differential equations describing electromagnetic field/defect interactions are extremely difficult to derive because of the inherently awkward defect boundary shapes and boundary conditions. In this study, conductivity variations in the weld region would make the analytic approach impractical. It is also difficult to carry out an experimental study of weld regions, since the machining of typical weld defects such as porosity, incomplete penetration etc., is complicated. Numerical modeling helps overcome these problems. Complicated boundary conditions are dealt with in a very elegant manner and the study of complicated defect shapes becomes relatively simple.

The finite difference method and the finite element method have been used extensively in dealing with partial differential equations [15,16]. The finite difference method involves discretization of the region into rectangular grids and then approximating the Poisson's equation by difference equations at the mesh points. These equations are solved iteratively to obtain the final solution. The drawbacks of this technique are the inability of the rectangular grid to model complex boundaries or defects and the time involved in the convergence of the solution. The finite element method has been used extensively in solving electromagnetic field problems. The finite element code in its axisymmetric, quasi-static form used in this work has been proven, by earlier studies [6, 17, 18, 19], to be

accurate and simple to use especially in axisymmetric tube studies. In this chapter, the formulation of the energy functional and its minimization, the discretization and the finite element solution are described. The computation of coil parameters from the magnetic vector potential is explained in the concluding part of this chapter.

4.2 Variational Finite Element Model

The general procedure employed in this approach is [20]:

1. Formulation of the energy functional
2. Discretization
3. Interpolation
4. Elemental formulation
5. Assembly
6. Constraints
7. Solution
8. Computation of derived or secondary variables

Each of these basic steps is now described.

4.2.1 Energy functional

The governing partial differential equation (PDE) for the quasi-static eddy current phenomenon, as shown in Chapter 3, is given by :

$$\nabla \times \frac{1}{\mu} \nabla \times \overline{A} = \overline{J}_s - j\omega\sigma \overline{A} \qquad (4.1)$$

The following assumptions have been made:

1. All quantities are ac phasors.
2. Eddy currents within the excitation coil itself can be neglected.
3. The material is homogenous and isotropic.
4. The displacement currents are negligible in comparison to the induced conduction current density.
5. Coulomb gauge, $\nabla . \overline{A} = 0$.

Equation 4.1 is a linear vector diffusion equation, which in the phasor domain is an elliptic PDE. The left-hand side of the equation represents the spatial variation of the magnetic vector potential. The right hand side consists of the source current density $\overline{J}_s$ and the eddy current density $-j\omega\sigma \overline{A}$ which is induced by the field in conducting structures present in the region of interest. The difference in sign between the source current density and the eddy current density is due to Lenz's law which states that **'the induced electromotive force (emf) tries to oppose the change in flux which produces it'.**

The finite element method does not solve the diffusion equation directly. The appropriate energy functional is computed and is then minimized to obtain the solution. The energy functional corresponding to the above diffusion equation can be obtained [6] using the Euler equation. Given the energy functional of the form

$$F = \int_R \int f(\overline{A}, A_r, A_z, r, z)\, r\, dr dz \qquad (4.2)$$

the corresponding Euler equation which has to be satisfied is given by

$$\frac{\partial}{\partial r}\left(\frac{\partial f}{\partial A_r}\right) + \frac{\partial}{\partial z}\left(\frac{\partial f}{\partial A_z}\right) - \frac{\partial f}{\partial \overline{A}} = 0 \qquad (4.3)$$

That is to say the energy functional is appropriate if the substitution of equation 4.2 in equation 4.3 yields the governing equation.

An energy functional corresponding to the diffusion equation of 4.1 is given by [6]

$$F = \int_R \int \left\{ \frac{1}{2\mu} \left[\left(\frac{\partial \overline{A}}{\partial r} + \frac{\overline{A}}{r} \right)^2 + \left(\frac{\partial \overline{A}}{\partial z} \right)^2 \right] + \frac{j\omega\sigma}{2} \left(\overline{A} \right)^2 - \overline{J}_s \cdot \overline{A} \right\} r\, dr\, dz \qquad (4.4)$$

4.2.2 Finite element discretization

Fig 4.1 shows how the mesh, in an axisymmetric case, could be treated as 'donut' shaped rings with triangular cross sections. Since the magnetic vector potential is independent of the direction of ϕ, just one half the cross section of the 'donut' can be considered [6]. Fig 4.2 shows a typical mesh for the geometry of a differential eddy current probe moving within a tube.

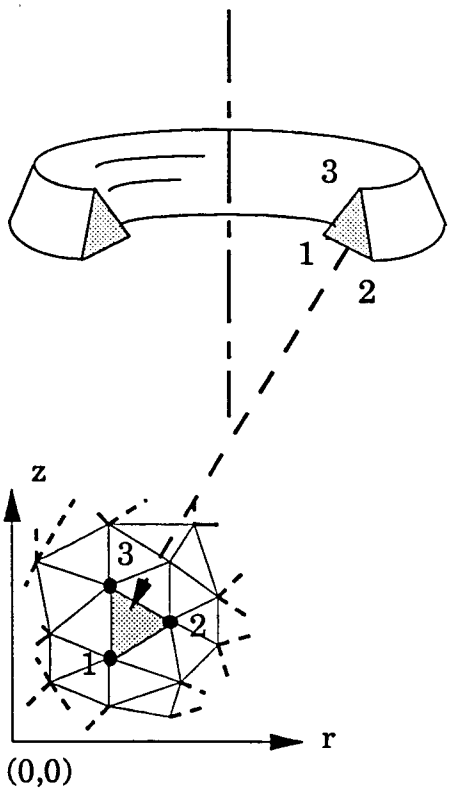

Fig 4.1 Spatial discretization of a two dimensional region using triangular elements [6]

4.2.3 Finite element formulation

We now have our solution region discretized into a mesh of triangles. Consider a single triangular element 1-2-3 as shown in Fig 4.1. The vector potential is assumed to be a linear function over the region of each triangle given by

$$\overline{A}_p = \overline{\alpha}_1 + \overline{\alpha}_2 r + \overline{\alpha}_3 z. \qquad (4.5)$$

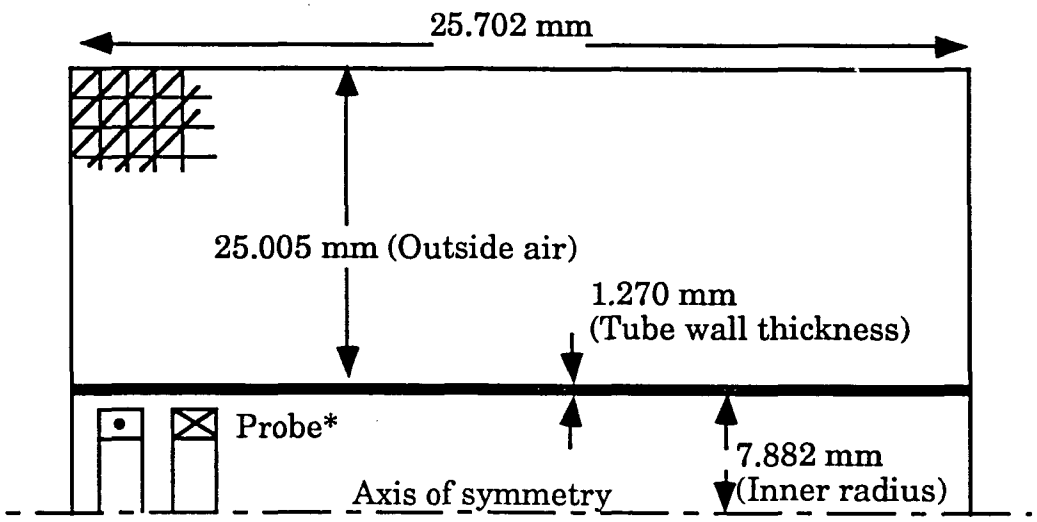

* Probe dimensions:
coil: 1.567 mm sq., lift-off: 0.263 mm, coil separation: 0.695 mm

Fig. 4.2 A typical mesh

The coefficients $\bar{\alpha}_1$, $\bar{\alpha}_2$ and $\bar{\alpha}_3$ are related to the values of the magnetic vector potentials $\bar{A}_1$, $\bar{A}_2$ and $\bar{A}_3$ at the vertices of the triangle as follows:

$$\begin{bmatrix} \bar{A}_1 \\ \bar{A}_2 \\ \bar{A}_3 \end{bmatrix} = \begin{bmatrix} 1 & r_1 & z_1 \\ 1 & r_2 & z_2 \\ 1 & r_3 & z_3 \end{bmatrix} \begin{bmatrix} \bar{\alpha}_1 \\ \bar{\alpha}_2 \\ \bar{\alpha}_3 \end{bmatrix} \qquad (4.6)$$

where (r_1, z_1), (r_2, z_2) and (r_3, z_3) are the coordinates of the vertices 1, 2 and 3 respectively.

The matrix can be inverted and the $\bar{\alpha}$'s become

$$\begin{bmatrix}\overline{\alpha}_1\\ \overline{\alpha}_2\\ \overline{\alpha}_3\end{bmatrix} = \frac{1}{2\Delta}\,[1\ r\ z]\begin{bmatrix}(r_2z_3 - r_3z_2) & (r_3z_{31} - r_1z_3) & (r_1z_2 - r_2z_1)\\ (z_2 - z_3) & (z_3 - z_1) & (z_1 - z_2)\\ (r_3 - r_2) & (r_1 - r_3) & (r_2 - r_1)\end{bmatrix}$$

$$\times \begin{bmatrix}\overline{A}_1\\ \overline{A}_2\\ \overline{A}_3\end{bmatrix} \qquad (4.7)$$

with

$$2\Delta = \begin{vmatrix}1 & r_1 & z_1\\ 1 & r_2 & z_2\\ 1 & r_3 & z_3\end{vmatrix} \qquad (4.8)$$

where Δ is the area of the triangle and $|\cdot|$ represents the determinant.

As shown by Chari [21] for the two dimensional case and by Brauer [22] for the axisymmetric case, the vector potential for each triangle, equation 4.7, is substituted into the energy functional, equation 4.4, and the functional is differentiated with respect to the unknown magnetic vector potentials $\overline{A}_1$, $\overline{A}_2$ and $\overline{A}_3$ and equated to zero. For an element 'e',

$$\frac{\partial F_e}{\partial \overline{A}_i} = \int\int_R \Big\{\frac{1}{\mu}\Big[\Big(\frac{\partial \overline{A}}{\partial r} + \frac{\overline{A}}{r}\Big) + \Big(\frac{\partial}{\partial \overline{A}_i}\frac{\partial \overline{A}}{\partial r} + \frac{\partial}{\partial \overline{A}_i}\Big(\frac{\overline{A}}{r}\Big) + \Big(\frac{\partial \overline{A}}{\partial z}\Big)\frac{\partial}{\partial \overline{A}_i}\frac{\partial \overline{A}}{\partial z}\Big]$$
$$+ j\omega\sigma\overline{A}\,\frac{\partial \overline{A}}{\partial \overline{A}_i} - \overline{J}_s\frac{\partial \overline{A}}{\partial \overline{A}_i}\Big\}\, r\, dr\, dz = 0; \qquad i = 1, 2, 3 \qquad (4.9)$$

4.2.4 Assembly and solution

Substituting equation 4.9 into the finite element approximation of equation 3.7 an element matrix equation results [6] which is of the form

$$\{[S]_e + j[R]_e\} [\overline{A}_e] = [\overline{Q}]_e \qquad (4.10)$$

where $[S]_e$ is a 3x3 'element' matrix formed from the r and z values of the three vertices 1, 2 and 3 and the μ value associated with element 1-2-3, and its area Δ. $[R]_e$ is a 3x3 constant element matrix formed from the angular frequency ω, the electrical conductivity s, and the area Δ associated with the element 1-2-3. $[\overline{Q}]_e$ is the 3x1 source element matrix formed from the complex source current density $\overline{J}_s$, within the element 1-2-3. $[\overline{A}_e]$ is a 3x1 matrix formed from the unknown magnetic vector potentials $\overline{A}_1$, $\overline{A}_2$ and $\overline{A}_3$. This matrix equation is the foundation of the axisymmetric finite element formulation of the energy functional for one triangular element in the solution region. The method is extended to all elements in the region and individual matrices combined to form a global matrix equation,

$$[G] [A] = [Q] \qquad (4.11)$$

The matrix [G] is an NxN banded symmetric complex matrix and [A] and [Q] are Nx1 complex matrices, where N is the total number of node points. A direct Gaussian elimination technique is used to invert [G] to obtain the vector potentials at each triangle vertex, or node point in the

solution region. The vector potential thus determined is the vector potential which minimizes the original energy functional. This approximation is almost indistinguishable from analytic solutions if the discretization is made very small.

4.3 Computation of Derived Variables

Once the magnetic vector potential is known, important parameters such as the eddy current density and the coil impedance can be obtained from further calculations.

If $\overline{\mathbf{A}}$ is the complex vector potential at a point in a conducting material, then the eddy current density at that point is given by

$$\overline{J}_e = -j\omega\sigma\overline{\mathbf{A}} \tag{4.12}$$

The phase angle lag to $\overline{J}_e$ is a function of $\overline{\mathbf{A}}$ and the depth into the conducting material for which it is calculated.

The impedance of a length of wire $\overline{dl}$ carrying an alternating current $\overline{I}_s$ (amps rms) is given by

$$\overline{Z} = \frac{j\omega \int_c \overline{\mathbf{A}} \cdot dl}{\overline{I}_s} \tag{4.13}$$

For axisymmetric fields the impedance of a circular loop of radius r_i can be calculated [6] from the magnetic vector potential $\overline{A}_i$ at r_i and the rms value of the impressed current $\overline{I}_s$ (amps) in the loop (Fig. 4.3). That is, using equation 4.13

$$Z_i = \frac{j\omega 2\pi r_i \overline{A}_i}{\overline{I}_s} \tag{4.14}$$

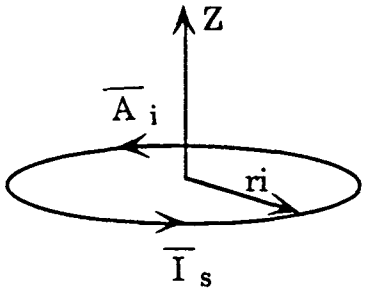

Fig. 4.3. Calculation of the impedance of circular loop [6]

Integration of equation 4.12 over all the turns in the circular coil provides the total impedance of the coil. For finite element studies the centroidal values $\overline{A}_{cj}$ and r_{cj} for the jth triangular element can be substituted instead of $\overline{A}_i$ and r_i without much loss in accuracy. If N_s is the uniform turn density (turns/m^2) in the source region, the total impedance of all turns in element j with area Δ_j is:

$$\overline{Z}_j = \frac{j\omega 2\pi r_{cj} \overline{A}_{cj} N_s \Delta_j}{\overline{I}_s} \tag{4.15}$$

where

$$\overline{A}_{cj} = \left[\frac{1}{12}\{\overline{A}_l^{\,2} + \overline{A}_m^{\,2} + \overline{A}_n^{\,2} + (\overline{A}_l + \overline{A}_m + \overline{A}_n)^2\}\right]^{1/2} \qquad (4.16)$$

and

$$r_{cj} = \left[\frac{1}{12}\{r_l^{\,2} + r_m^{\,2} + r_n^{\,2} + (r_l + r_m + r_n)^2\}\right]^{1/2} \qquad (4.17)$$

Hence the total impedance of a circular coil whose cross section is discretized into N triangular elements is given (considering $N_s \overline{I}_s = \overline{Js}$) by,

$$\overline{Z}_j = \frac{j\omega 2\pi \overline{J}_s}{\overline{I}_s^{\,2}} \sum_{j=1}^{N} (r_{cj}\Delta j)\,\overline{A}_{cj} \qquad (4.18)$$

For a differential probe with two coils similar in construction and carrying the same amount of current (in opposite directions) the total impedance of the probe is obtained by algebraically summing up their individual impedances. Hence

$$\overline{Z}_{probe} = \frac{j\omega 2\pi \overline{J}_s}{\overline{I}_s^{\,2}} \left[\sum_{j=1}^{N_b} (r_{cj}\Delta j)\,\overline{A}_{cj} + \sum_{j=1}^{N_a} (r_{cj}\Delta j)\,\overline{A}_{cj}\right] \qquad (4.19)$$

Usually, the coil impedance is normalized to the magnitude of the coil impedance in air. That is, the coil is modeled with no conducting media in the solution region, and the coil impedance in air is given by [6]

$$L_0 = \frac{\overline{Z}_{coil}}{j\omega} = \frac{2\pi \overline{J}_s}{\overline{I}_s^{\,2}} \sum_{j=1}^{N} (r_{cj}\Delta_j)\, \overline{A}_{cj} \tag{4.18}$$

where N is the total number of finite elements in the finite element cross section.

Calculation of the above quantities enables the plotting of the probe impedance plane trajectories and comparison with experimental results. Also, the magnetic vector potentials calculated can be used to obtain flux plots to study the energy defect interaction.

5 FEATURE EXTRACTION AND CLASSIFICATION

5.1 Introduction

Recognizing patterns independent of phase rotation, scaling and translation has been the focus of much recent research [1,23]. In the current study an automated scheme to classify the defect and weld signals from tubing independent of the magnitude and translation of the signal is the next logical step after obtaining the impedance plane trajectories. This invariance is required so as to make the classification insensitive to the starting point of the impedance plane trajectories and also to magnitude of the trajectory, since in this preliminary classification scheme proposed sizing of the flaw is not included. Extracting features invariant under rotation, scaling and translation is one way of achieving this end. Feature extraction is an important aspect in nondestructive testing processes. Apart from achieving invariance, data reduction is also achieved. Numerous methods for feature extraction have been used with excellent results in different applications. Recognition of patterns and classifying them into respective classes is another much researched field. In this chapter a discussion of a few important methods of feature extraction is given. The multilayer perceptron (MLP) trained using the back propagation training algorithm is discussed as a pattern classifier. The Fourier descriptors and invariant moments as features in weld identification with the MLP are described.

5.2 Feature Extraction

Representation of a signal is sometimes done by just storing the raw data. This however is not a very efficient approach. For purposes of data compression and for incorporation into a learning algorithm, feature extraction becomes essential. It is important that the features selected as descriptors be as insensitive as possible to such variations as change in size, translation and rotation. In the present study, for example, the impedance plane trajectory would have different magnitudes for defects of the same type but of different sizing. Also, depending on the starting point, signals from the same defect type could be translated in position. Hence it is required to use features insensitive to translation and scaling. A number of approaches, some of them tailored to specific applications, have been suggested [1]. Broadly speaking the features extracted could be parametric or nonparametric in nature [1]. What follows is a brief discussion of the two types.

5.2.1 Parametric signal processing

A great deal of attention is now being focused on parametric approaches because of relative advantages over nonparametric methods such as the ability to reconstruct the signal from the parametric features [1]. The general procedure involves selection of a suitable model for representing the signal. Model coefficients are then identified using established performance criteria [1]. The model coefficients uniquely

represent the signal. Also, the method can be incorporated very easily into a learning system.

A variety of parametric models have been developed in the past which cater to a wide variety of applications. This thesis however confines its attention to the Fourier descriptor method of characterizing impedance plane trajectories.

5.2.2 Nonparametric Signal Processing

In nonparametric approaches the signal is characterized by a few heuristic parameters which are expected to contain information that would enable discrimination between signals belonging to different classes. In general the heuristic nature of the parameters does not allow reconstruction of the signal [1]. The sole index of performance is then the ability to discriminate between defects.

The invariant moments technique is a nonparametric approach which has shown promise in the identification of closed curves. This method exploits the fact that certain functions of moments of a two dimensional pattern are invariant under rotation, translation and scaling. Using this approach the reconstruction of the signal is difficult but possible. In this thesis the effectiveness of invariant moments in weld identification is studied.

5.2.3 Fourier descriptors

Of the several types of Fourier descriptors suggested, only the set defined by Granlund [24] is discussed in this thesis.

Consider a simply closed curve as shown in Fig. 5.1.

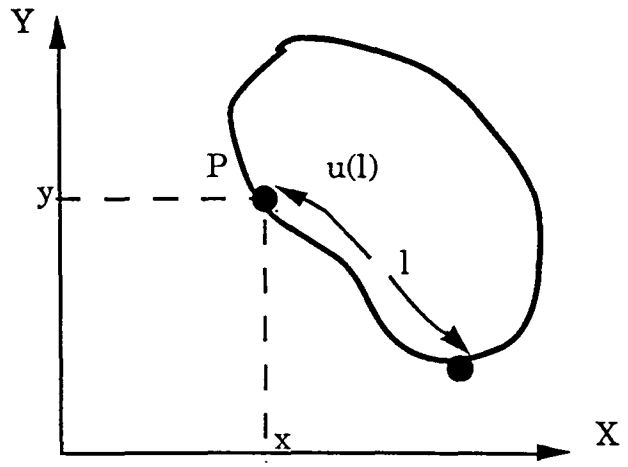

Fig. 5.1 Point moving along a closed curve.

Consider a point moving along the boundary of the curve - $Z(l) = (x(l), y(l))$ in the clockwise direction generating the complex function $u(l) = x(l) + iy(l)$. The complex function is periodic with period L, where L is the length of the curve.

$$\text{i.e., } u(t+nL) = u(t) \qquad (5.1)$$

where t is an arbitrary variable and n= 0, 1, 2 ...

Hence u(l) can be expanded in a Fourier series [1]:

$$u(l) = \sum_{n=-\infty}^{\infty} c_n \, e^{i(2\pi/L)\, nl} \qquad (5.2)$$

From which the coefficients are obtained as:

$$c_n = \int_0^l u(l) \; e^{i(2p/L)\, nl} \, dl \qquad (5.3)$$

The coefficients are however not invariant under rotation, translation, scaling and choice of starting point. Functions of these coefficients which are invariant under these transformations can however be derived. One such function is given by

$$b_n = \frac{c_{1+n}\, c_{1-n}}{c_1^2} \qquad (5.4)$$

Without going into the proof, it is stated that b_n is invariant under the transformations mentioned earlier and hence can be used as features [1]. The number of Fourier descriptors required to represent a signal is largely a function of the permissible error. Seven Fourier descriptors and the phase angle have been used as a feature vector in this study to represent the impedance plane trajectories.

5.2.4 Invariant moments

In classical mechanics and statistical theory the concept of moments is used extensively; concepts of central moments, size normalization, and principal axes are also used [25]. The two dimensional moment invariants and their applications in visual pattern recognition are presented by Ming-Kuei Hu [23].

Given a two dimensional continuous function f(x, y) we define the moment of order (p+q) by the relation

$$m_{pq} = \int_{-\infty}^{\infty}\int_{-\infty}^{\infty} x^p y^q f(x,y)dxdy \qquad (5.5)$$

for p,q = 0, 1, 2, ...

A uniqueness theorem (Papoulis [1965]) states that if f(x, y) is piecewise continuous and has nonzero values only in a finite part of the x-y plane, then the moments of all orders exist and the moment sequence (m_{pq}) is uniquely determined by f(x, y). Conversely, m_{pq} uniquely determines f(x, y). The central moments can be expressed as

$$\mu_{pq} = \int_{-\infty}^{\infty}\int_{-\infty}^{\infty} (x - x')^p (y - y')^q f(x, y)\, dx\, dy \qquad (5.6)$$

$$\text{where } x' = \frac{m_{10}}{m_{00}}, \quad y' = \frac{m_{01}}{m_{00}} \qquad (5.7)$$

For digital images the central images are given by

$$\mu_{pq} = \sum_{-\infty}^{\infty} \sum_{-\infty}^{\infty} (x - x')^p (y - y')^q f(x,y) dxdy \qquad (5.8)$$

Using the above expression, expressions for central moments of order 3 can be written and expressed in terms of simple moments. In summary,

$$\mu_{00} = m_{00}$$
$$\mu_{10} = 0$$
$$\mu_{01} = 0$$
$$\mu_{20} = m_{20} - x' m_{10}$$
$$\mu_{02} = m_{02} - y' m_{01}$$
$$\mu_{11} = m_{11} - y' m_{10}$$
$$\mu_{30} = m_{30} - 3x' m_{20} + 2m_{10} x'^2 \qquad (5.9)$$
$$\mu_{03} = m_{03} - 3y' m_{02} + 2m_{01} y'^2$$
$$\mu_{12} = m_{12} - 2y' m_{11} - m_{02} x' + 2y'^2 m_{10}$$
$$\mu_{21} = m_{21} - 2x' m_{11} - m_{20} y' + 2x'^2 m_{01} \qquad (5.10)$$

The central moments are invariant to translation. Moments that are invariant under other transformations also may be developed as follows.

The normalized central moments, denoted by η_{pq} are defined as

$$\eta_{pq} = \frac{\mu_{pq}}{m^{\gamma_{00}}} \qquad (5.11)$$

where

$$\gamma = \frac{p+q}{2} + 1 \qquad (5.12)$$

for $p + q = 2, 3, ...$

From the second and third moments, a set of seven invariant moments can be derived [23, 32]. They are given by

$$\phi_1 = \eta_{20} + \eta_{02}$$

$$\phi_2 = (\eta_{20} - \eta_{02})^2 + 4\eta^2_{11}$$

$$\phi_3 = (\eta_{30} - 3\eta_{12})^2 + (3\eta_{21} - \eta_{03})^2$$

$$\phi_4 = (\eta_{30} + \eta_{12})^2 + (\eta_{21} + \eta_{03})^2$$

$$\phi_5 = (\eta_{30} - 3\eta_{12})(\eta_{30} + \eta_{12})[(\eta_{30} + \eta_{12})^2 - 3(\eta_{21} + \eta_{03})^2]$$
$$+ (3\eta_{21} - \eta_{03})(\eta_{21} + \eta_{03})[3(\eta_{30} + \eta_{12})^2 - (\eta_{21} + \eta_{03})^2]$$

$$\phi_6 = (\eta_{20} - \eta_{02})[(\eta_{30} + \eta_{12})^2 - (\eta_{21} + \eta_{03})^2] + 4\eta_{11}(\eta_{30} + \eta_{12})(\eta_{21} + \eta_{03})$$

$$\phi_7 = (3\eta_{21} - \eta_{03})(\eta_{30} + \eta_{12})[(\eta_{30} + \eta_{12})^2 - 3(\eta_{21} + \eta_{03})^2]$$
$$+ (3\eta_{12} - \eta_{30})(\eta_{21} + \eta_{03})[3(\eta_{30} + \eta_{12})^2 - (\eta_{21} + \eta_{03})^2] \qquad (5.13)$$

This set of moments has been shown to be invariant to translation, rotation, and scale change. In this project the set of seven invariant moments along with the phase angle have been used as an eight feature input vector. It should be pointed here that the term phase of the impedance plane trajectory in this study has been used to refer to the angle between the positive x-axis and the line joining the origin and the point of maximum

amplitude of the impedance plane trajectory in the positive y-axis direction (Fig. 3.3).

5.3 Classification

Once we have a feature vector the next stage is to incorporate it into a classification scheme. In this thesis the multilayer perceptron has been studied.

5.3.1 Multilayer perceptron

A multilayer perceptron can form any, possibly unbounded, convex region in space spanned by the inputs [26]. The capabilities of a multilayer perceptron stem from the nonlinearities within the node. A three layer perceptron [26] can form arbitrarily complex decision regions and can separate meshed classes. Hence no more than three layers are required in perceptron-like feed-forward nets.

The perceptron developed in this study is double layered. It has an input layer with eight nodes, a hidden layer with four nodes, and an output layer with two nodes as shown in Fig.5.2. The multilayer perceptron is totally interconnected (not all connections are shown in Fig. 5.2).

The output of the hidden layer is given by

$$x_j = f\left(\sum_{i=0}^{N-1} w_{ij} x_i - \theta_j \right) \qquad (5.14)$$

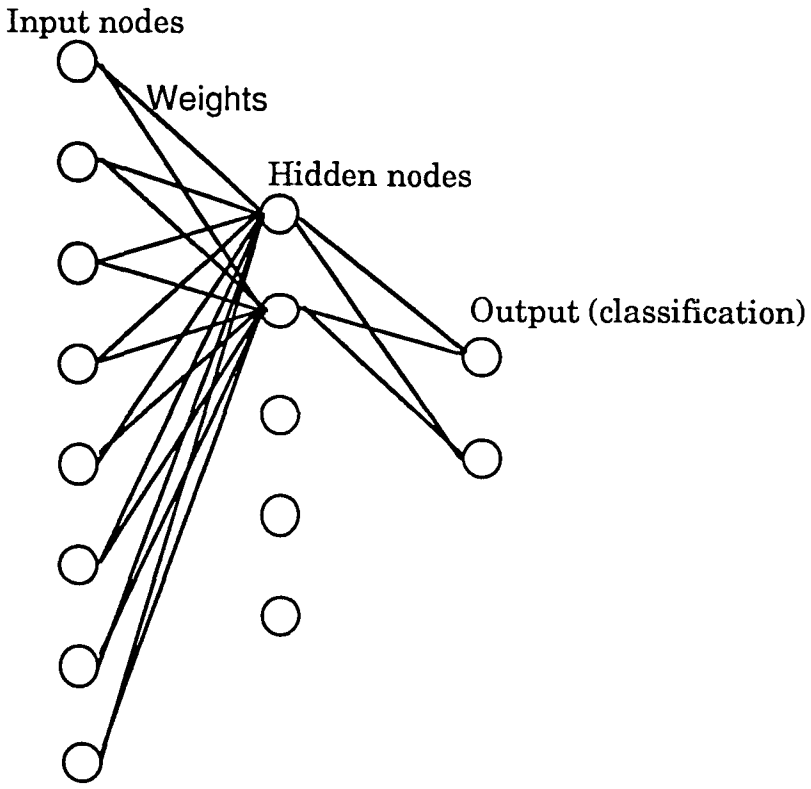

Fig. 5.2 A two layer perceptron.

And the output of the classification layer is given by:

$$y_l = f\left(\sum_{j=0}^{N_1-1} w'_{jl}\, x_j - \theta'_l \right) \qquad (5.15)$$

where w_{ij} are the connection strengths from the output to the hidden layer, and w_{jl} are the connection strengths from the hidden layer to the output

layer. θ_j and θ'_l are the internal offsets in those layers. f is the nonlinearity which is described in the next section.

5.3.2 The back-propagation training algorithm

The back-propagation training algorithm is an iterative gradient algorithm designed to minimize the mean square error between the actual output of a multilayer feed-forward perceptron and the desired output.

The algorithm can be summarized in five steps [26]:

- Step 1: Initialize weights.

- Step 2: Present inputs and desired outputs.

- Step 3: Calculate actual outputs using the sigmoid nonlinearity

$$f(\alpha) = 1/ (1 + e^{-(\alpha - \theta)}) \tag{5.16}$$

and the equations in the previous section.

- Step 4: Adapt weights.

Start at output nodes and work back to the first hidden layer

$$w_{ij}(t+1) = w_{ij}(t) + \eta\delta_j x_i' \tag{5.17}$$

where δ_j is the error term. If node j is an input node, then

$$\delta_j = y_j(1 - y_j)\,(d_j - y_j) \qquad (5.18)$$

where d_j is the desired output and y_j the actual output.

If node j is an internal hidden node, then

$$\delta_j = x_j'\,(1 - x_j')\sum_k \delta_k w_{jk} \qquad (5.19)$$

where k is over all nodes in the layers above node j.

- Step 5: Repeat by going to step 2.

The back-propagation algorithm basically calculates the error at the output layer and propagates it back through the previous layers adapting the weights to minimize the error. The method has repeatedly been proven to be excellent for training the multilayer perceptron [26].

The work described in this thesis is basically the study of weld regions and not classification of tubing defects. However, differentiating weld signals from other signals is an important aspect of studying weld regions. The study of the heat exchanger tubing (Chapter 1), which is the main motivation of this study, also calls for a classification scheme to differentiate the various defects. A brief description of the results obtained in classifying weld, crack and support plate signals is given in Chapter 7.

6 EXPERIMENTAL MEASUREMENTS

6.1 Overview of the Test System

Experimental measurements reported in Chapter 7 are made using a completely automated system. Fig. 6.1 gives a block diagram of the automated test system. The motor/controller combination sets the probe into motion. A computer controlled indexer card provides pulse signals to the controller which in turn generates signals that control the motor motion. The probe can be made to move to any particular position and stop, move between two positions, or made to perform a combination of the various moves. Simultaneously, the A/D converter digitizes the probe signal, the sampling frequency and the number of samples being user specified. The PC stores the sampled values. Filtering and processing of the data is then done on the PC. Hard copies are taken on the printer.

A brief description of each of the hardware components is given in the following paragraphs.

6.2 The Computer

Storing, displaying and analyzing the impedance plane trajectories necessitates the use a fast computer with good memory and computing facilities. This project uses a Hewlett Packard - Vectra 386.

Important features include: A 40MB hard disk, which is adequate memory for the purposes of storing impedance plane trajectory data files

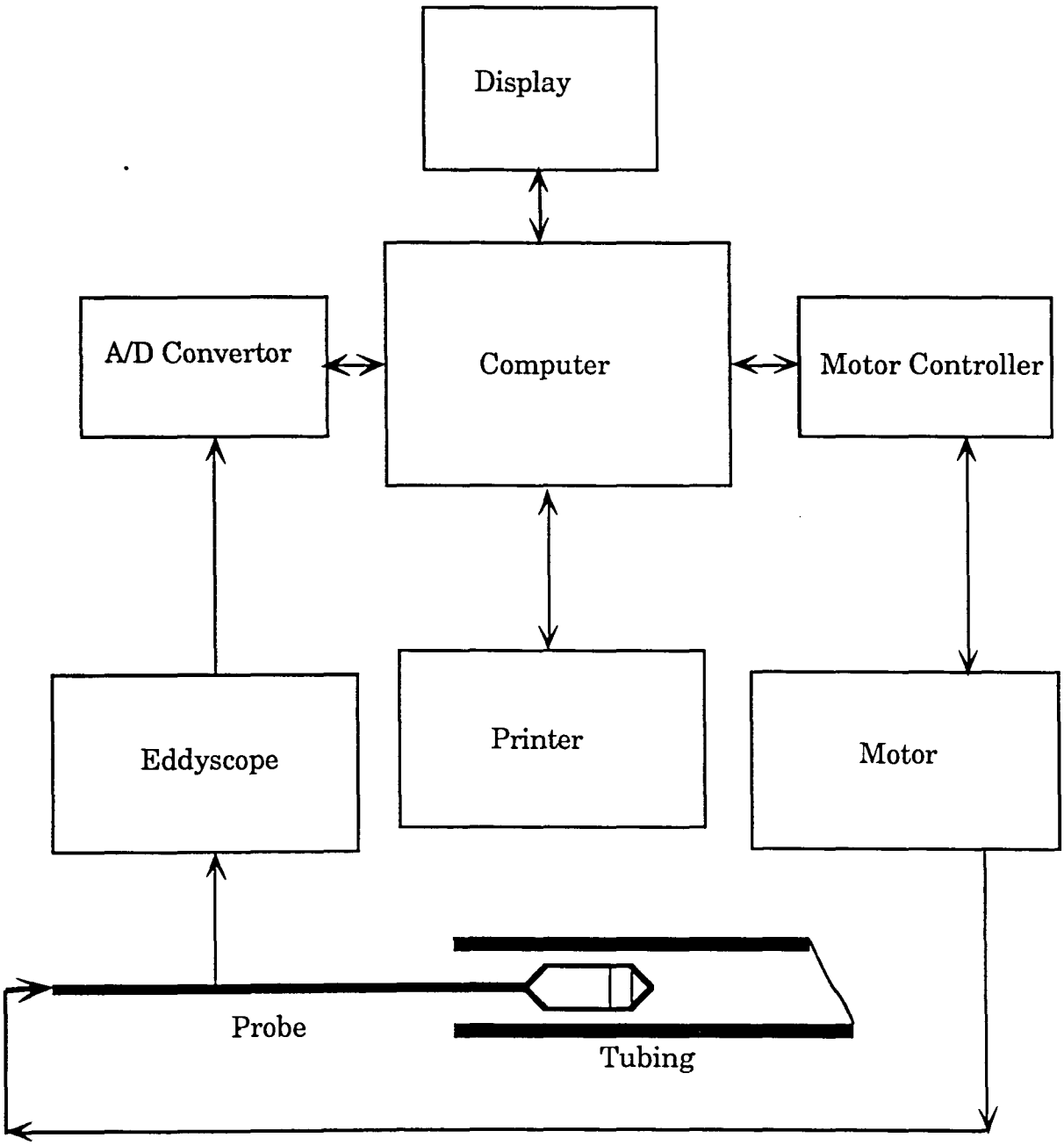

Figure 6.1. Test System

and the software for the application. Also available is a 3.5" floppy drive and a 5.25" floppy drive for additional storage. A math co-processor was

installed to provide for faster computational speed. Three serial ports and two parallel ports provide communication to the various peripherals shown in Fig. 5.1.

6.3 The A/D Converter

The A/D converter used to digitize the impedance plane trajectories was an RC Electronics ISC - 16 board. Features include: A 12 bit, 1 μsec A/D conversion which provides good accuracy and speed. A 1 to 16 channel programmable input multiplexer allows up to 16 channels to be digitized at the same time. For the present study two channels were used, one to digitize the imaginary part of the eddyscope impedance plane trajectory and the other to digitize the real part. The A/D conversion could be triggered by any of the channels being used by using an external trigger or an internal trigger. The triggering could be initiated by slope, level or threshold. In this project the A/D converter has been set to trigger when the eddyscope signal exceeds a preset threshold.

6.4 The Motor/Controller

A block diagram of the motor/controller is given in Fig. 6.2. Features of the different components are given:

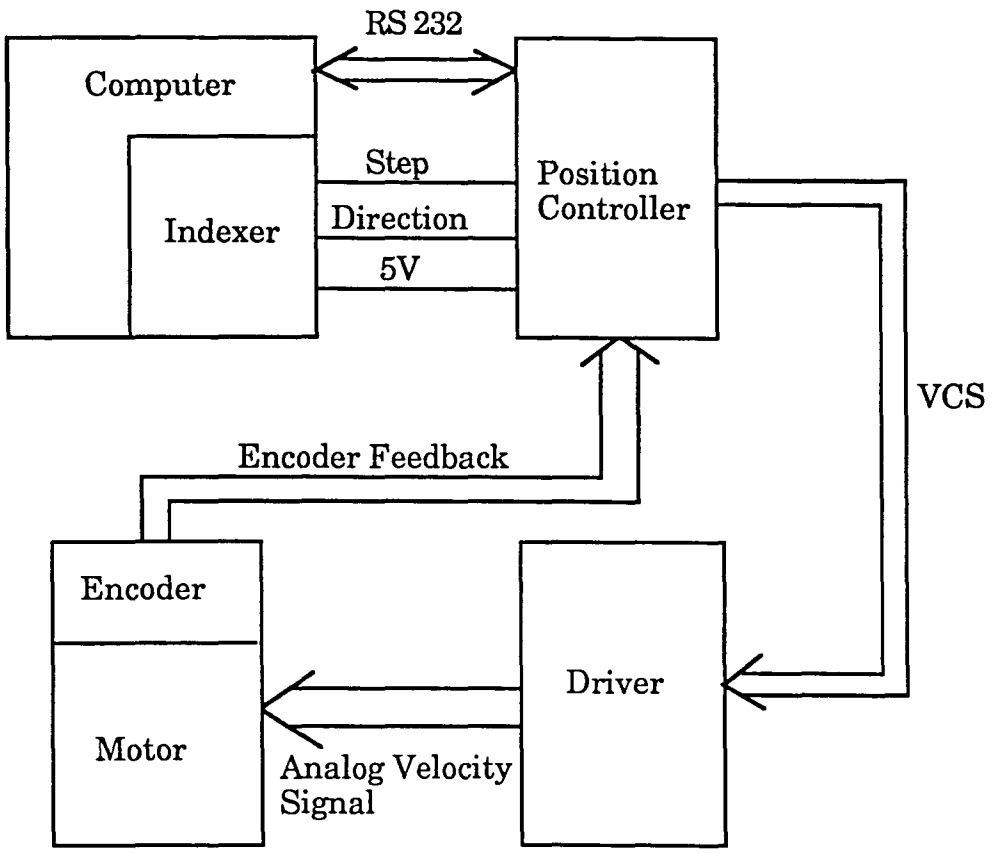

Figure 6.2 Details of the motor/controller

6.4.1 Indexer card

The indexer card is a board level product inserted into an open slot on a PC system expansion slot. The indexer card used was Compumotors' PC 21. The basic functions of the indexer include providing pulses to move the probe to a precise position and stop, or to move the probe at a constant velocity, or to move it between two points. The number of pulses decides the

distance the probe would move and the pulse-width decides the acceleration and velocity of motion.

6.4.2 Pulse input positioner

The pulse input positioner is a closed loop servo drive controller. The positioner used was Electrocraft's PRO-100. The pulse input positioner accepts the step (pulse) and direction signals from the indexer card, the encoder provides the position feedback. Depending on these two pieces of information the pulse input positioner outputs a velocity command signal (VCS) which is a dc signal proportional to the desired velocity of the motor, to the motor driver.

6.4.3 Pulse width modulated servo amplifier

The pulse width modulated servo amplifier is a dc switching type servo amplifier which interfaces with the controller described in the previous section, to provide the input analog velocity signal to the motor. The magnitude of this signal is proportional to the actual instantaneous motor speed. The servo amplifier used was Electrocraft's MAX-100.

6.5 Gas Tungsten Arc Welding

The tube specimens for the experimental tests were welded using the gas tungsten arc welding (GTAW) technique. The GTAW technique is an

arc process which uses a virtually nonconsumable tungsten electrode and an externally supplied inert atmosphere [27] (argon in our case).

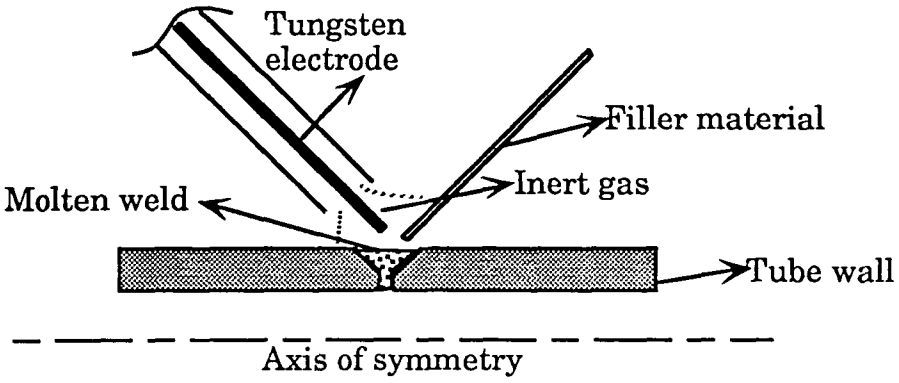

Fig. 6.3 Gas tungsten arc welding

Electricity, when passed through the small cross section tungsten electrode, produces high temperatures since tungsten is a poor conductor. This high temperature melts the parent material and the filler wire being fed, which then fuse to form the weld. The inert gas shields the molten metal from contaminants in the air. Fig. 6.3 shows a simple representation of the GTAW process.

7 RESULTS

7.1 Introduction

In an effort to study the feasibility of using the differential probe eddy current technique in weld inspection, and also to understand the physical structure, a study was made of both numerical and experimental signals.

The weld region parameters of importance are:

1. The conductivity of the parent material
2. The conductivity of the weld region
3. The conductivity of the heat affected zone (HAZ)
4. The dimensions of the various regions
5. The type of weld cut used.

The numerical model using the finite element approach was developed by varying the above parameters to obtain as close a match between the theoretical and experimental signals as possible. The different parameters were varied based on rough estimates obtained from an a priori knowledge of the type of weld, the materials being welded and the filler material being used. A reliable model based on verification from a large set of experimental results is a powerful tool to study the weld regions.

The numerical model could be put into use in a wide variety of ways. In order to obtain sizing and location of a weld defect, the position and size of the defect in the numerical model could be varied to obtain a close match to the experimental defect signal. The position and sizing of the defect can

be considered to be approximately the same as that obtained for the model. This is an extremely important aspect of this approach as previous researchers have concluded that a reliable sizing of weld defects was not possible using the eddy current approach [12]. Also, once a numerical model is obtained, numerically simulated signals for defects difficult to machine experimentally can be produced. Large data sets required to train neural networks in defect recognition can be generated using the model. What follows is a discussion of some of the important results obtained in this study.

7.2 Consistent Signals from Good Welds

The first step in studying the feasibility of using the differential probe eddy current method in weld testing is to see if good welds produce impedance plane trajectories of consistent shape, magnitude and phase. Experimental signals obtained from inconel tubes welded together using the Gas Tungsten Arc Welding (GTAW) method with stainless 308 as filler, are shown in Fig 7.1. An important point to note is that these signals were obtained from tubes which were cut and welded back together; that is to say the conductivity of the material on either side of the weld is exactly the same other than for the heat affected zones. The signals were obtained using the differential probe at a frequency of 400 KHz. The tube and probe dimensions are similar to those shown in Fig.4.2. The skin depth at this frequency was around 0.6 mm. The signals obtained are more or less consistent in terms of phase, magnitude, and shape. This result is encouraging since it is now

feasible to think in terms of discerning these signals from those produced by defective welds - assuming that the defects in the welds would affect the signal in terms of magnitude, phase or shape.

7.3 The Weld Model

The weld model was tuned using finite element simulations to match the experimental results in terms of shape and phase as mentioned earlier. The model obtained is shown in Fig. 7.2. Fig. 7.2 indicates the relative dimensions of the weld region, the heat affected zone, and the tube wall thickness. This model for the weld region was obtained by comparing a large number of experimental signals obtained from good welds with numerical simulations. A comparison of the simulated and experimental signals for a good weld is shown in Fig. 7.3. The conductivity in the weld region was taken to be in between that of the parent inconel tube (0.1400×10^4 siemens/mm) and the 308 steel filler material (0.1000×10^4 siemens/mm). The final model was obtained by changing the weld region conductivity, the conductivity in the heat affected zone and the width of the heat affected zone. In general, it was found that the shape of the weld region and the extent of the heat affected zone affect the shape of the IPT whereas the conductivity in the weld region affects the phase and amplitude of the IPT. To give an idea of how variations of the different variables affect the signal, numerical simulations for a weld model with a weld region conductivity 50% higher than that of the parent inconel material are shown in Fig. 7.4. Also, the heat affected zone was excluded

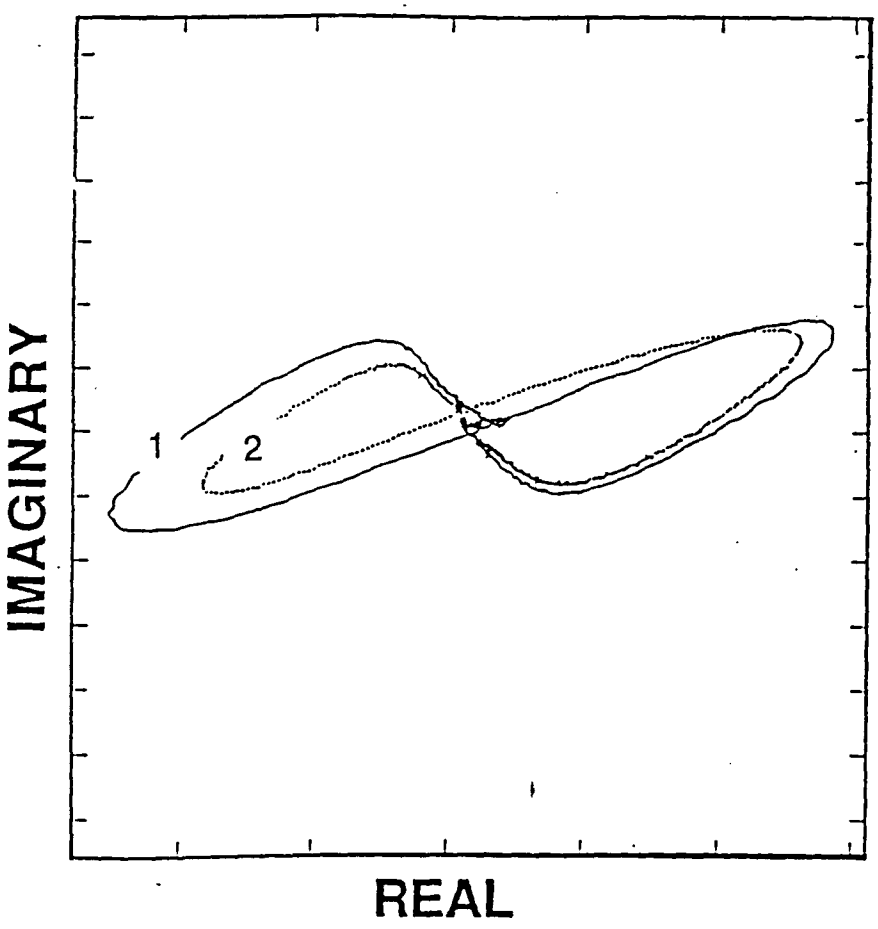

Fig. 7.1 Experimental signals from good welds (1 & 2 are signals from two welds)

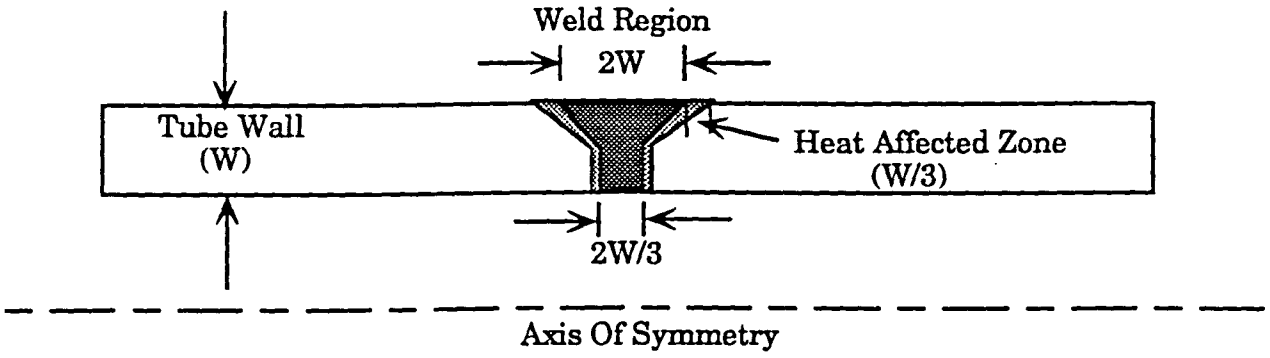

Fig. 7.2 A weld model

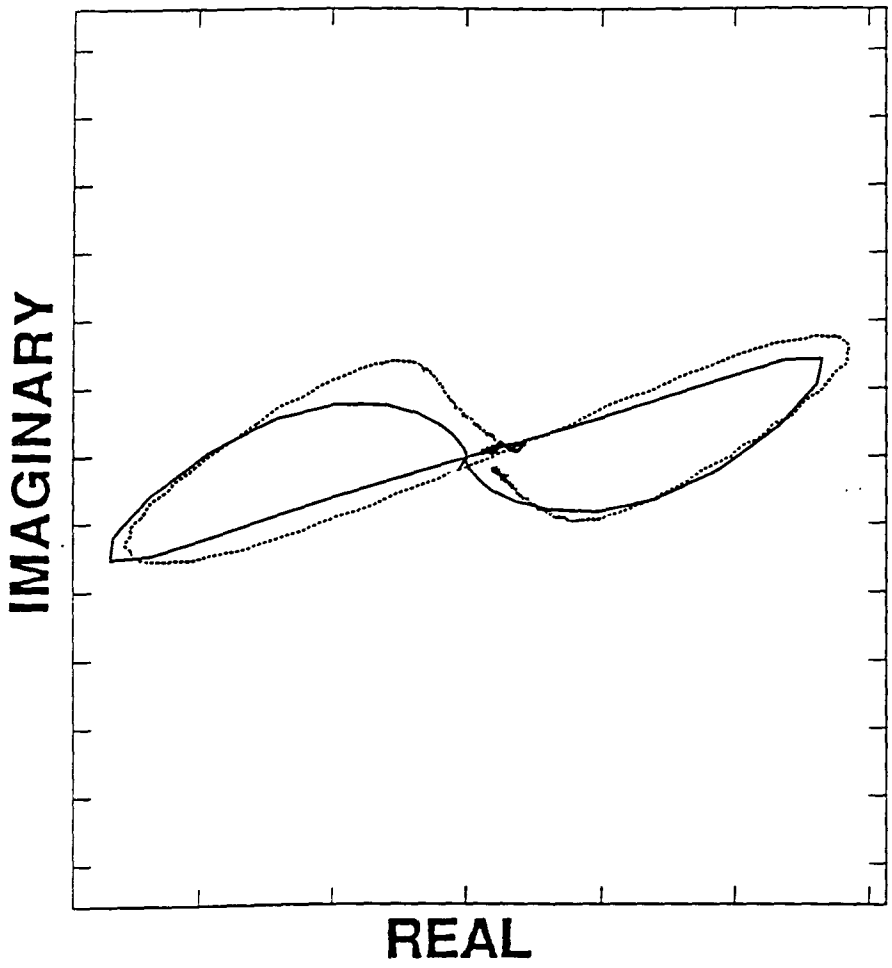

Fig. 7.3 Good weld: 1. Experimental, 2. Simulation

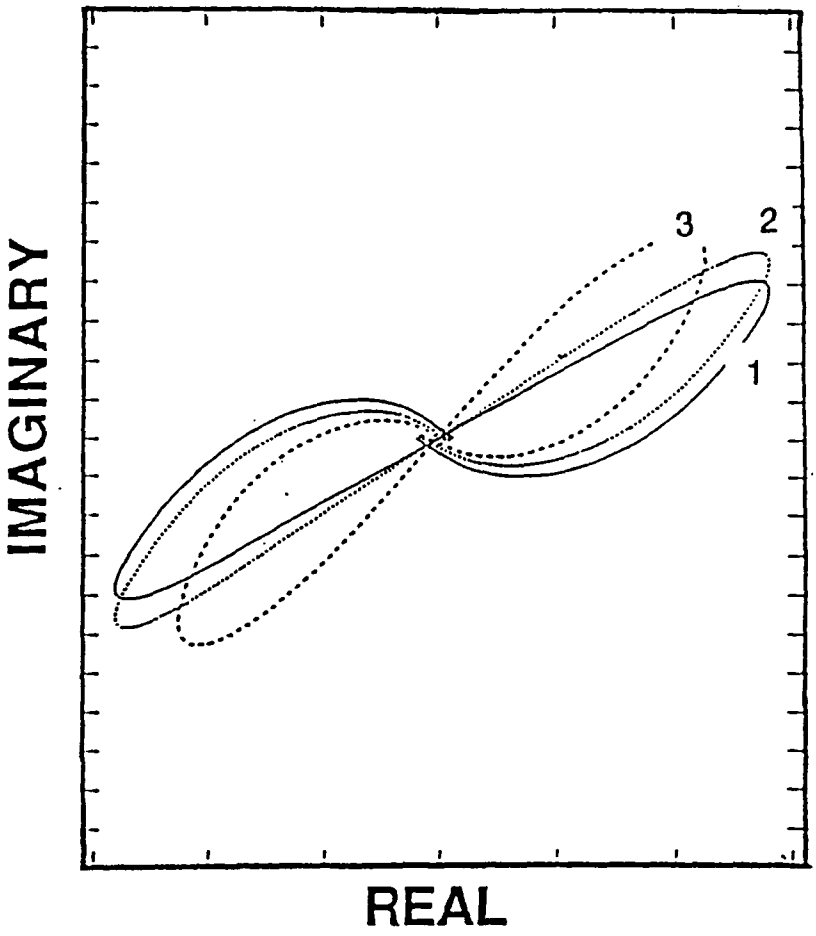

Fig. 7.4 Simulations with a bad model: 1. Good weld, 2. Crack in weld, 3. A bigger crack

in the model for these simulations. Shown in the figure are numerical simulations for such a model with growing crack depth. As can be seen, the shape of the good weld signal does not match very well with the experimental results of Fig. 7.1. Also, the crack growth in the model does not simulate the results described in section 7.4. It was found that a better match of the shape of the IPT was obtained by incorporating a heat affected zone of dimensions shown in Fig. 7.2 and a conductivity of around 10% lower than that of the parent material. Also, using a conductivity of around 0.1200×10^4 siemens/mm, the relative magnitude increase for the case of crack growth matches well with the experimental results as described in section 7.4.

7.4 Detection of Cracks in Welds

Cracks were artificially machined into the welds using a thin tube cutter. Experimental signals obtained are as shown in Fig. 7.5. As seen in the figure there is a distinct increase in both phase and magnitude with increasing depth of the crack. Cracks were simulated in the numerical model and similar changes in phase and magnitude were obtained. The simulated results which best matched the experimentally obtained results are shown in Fig. 7.6 and the defect dimensions for which this match was obtained are shown in Fig. 7.7. The phase changes and the amplitude changes depend on the frequency of operation. Also, the numerical studies indicate that the increase or decrease of the phase angle with increasing

defect dimensions is largely a function of the conductivity difference between the filler material and the parent material.

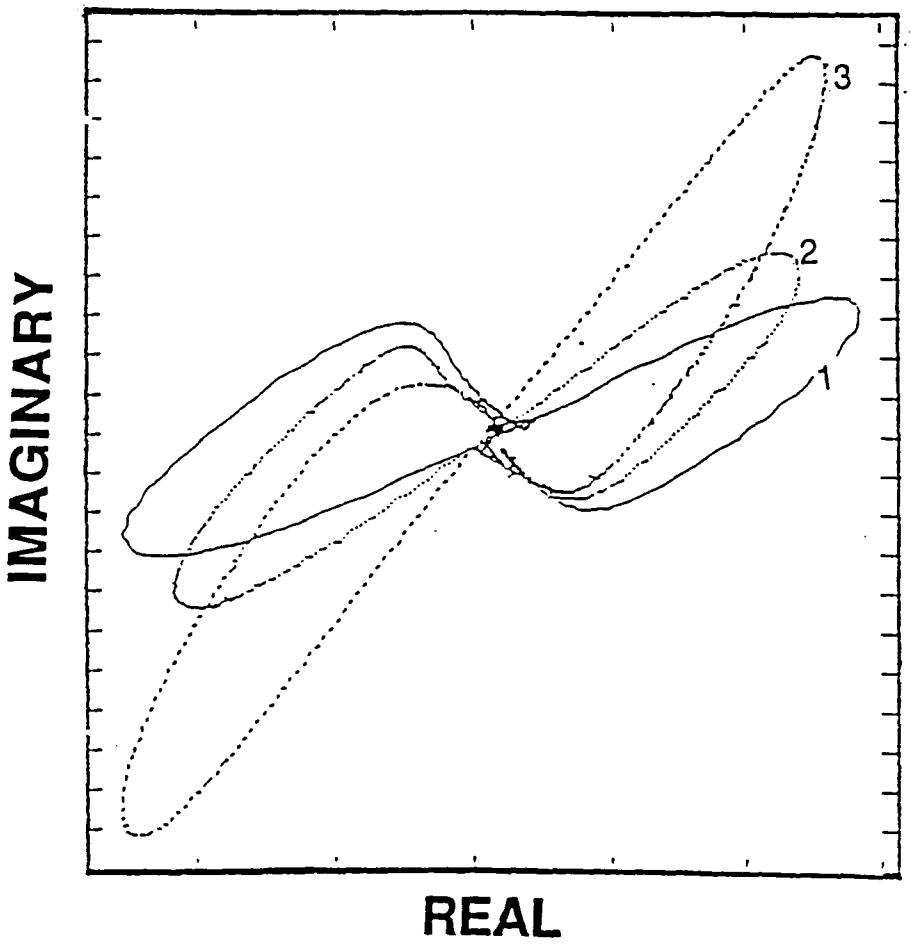

Fig. 7.5 Crack growth - experimental: 1. Good weld, 2. Crack in welds, 3. A deeper crack

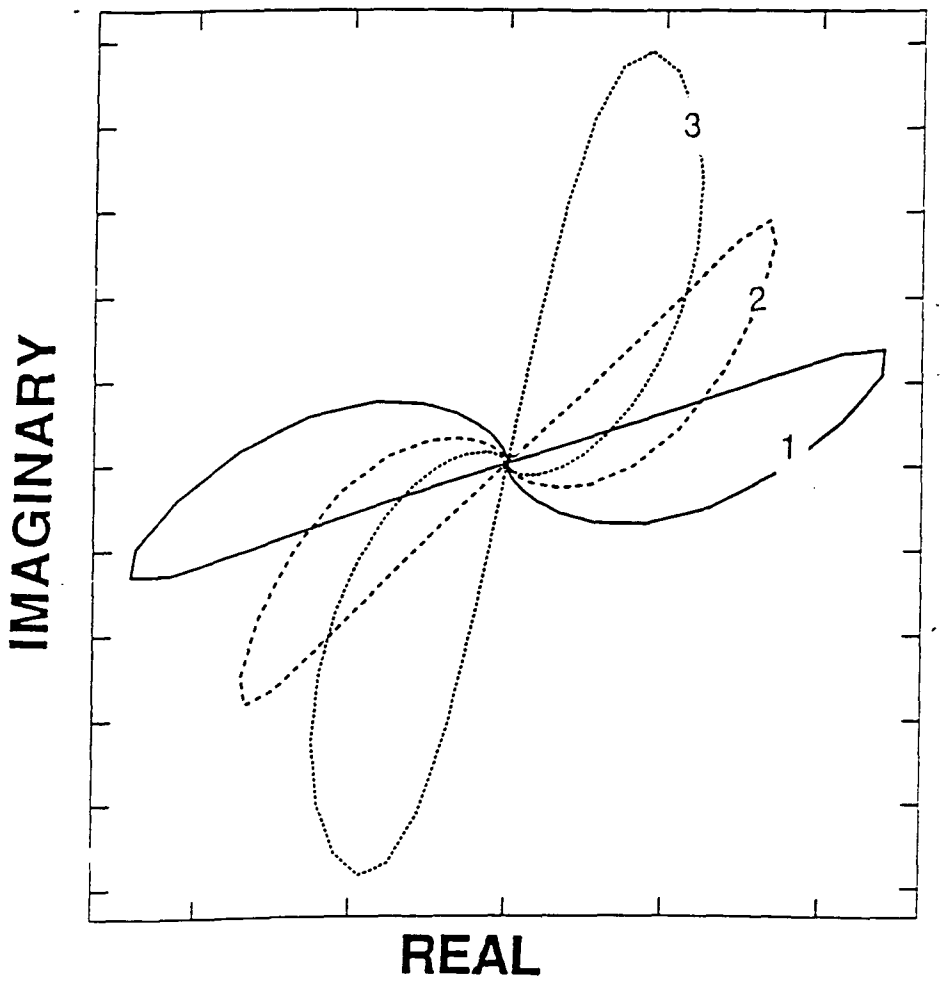

Fig. 7.6 Crack growth - simulated: 1. Good weld, 2. Crack in welds, 3. A deeper crack

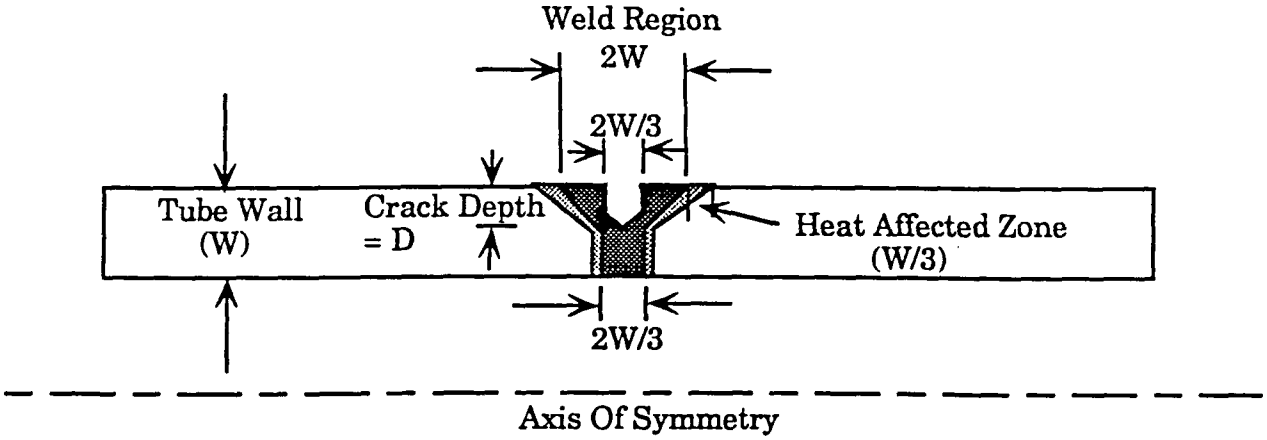

Crack Dimension corresponding to Figure 7.4:
1. D = 0
2. D = W/5
3. D = W/3

Fig. 7.7 Crack dimensions

7.5 Detection of Other Defects

The experimental signal obtained in the case of incomplete penetration is shown in Fig. 7.8. The corresponding numerical result is shown in Fig. 7.9. These signals are entirely different from those obtained from good welds and hence can be easily differentiated. Porosity is a defect type difficult to machine experimentally. Signals from welds with porosity were studied using the numerical model and the results obtained are shown in Fig. 7.10. As these results indicate, porosity in a weld can be detected using the differential probe eddy current technique.

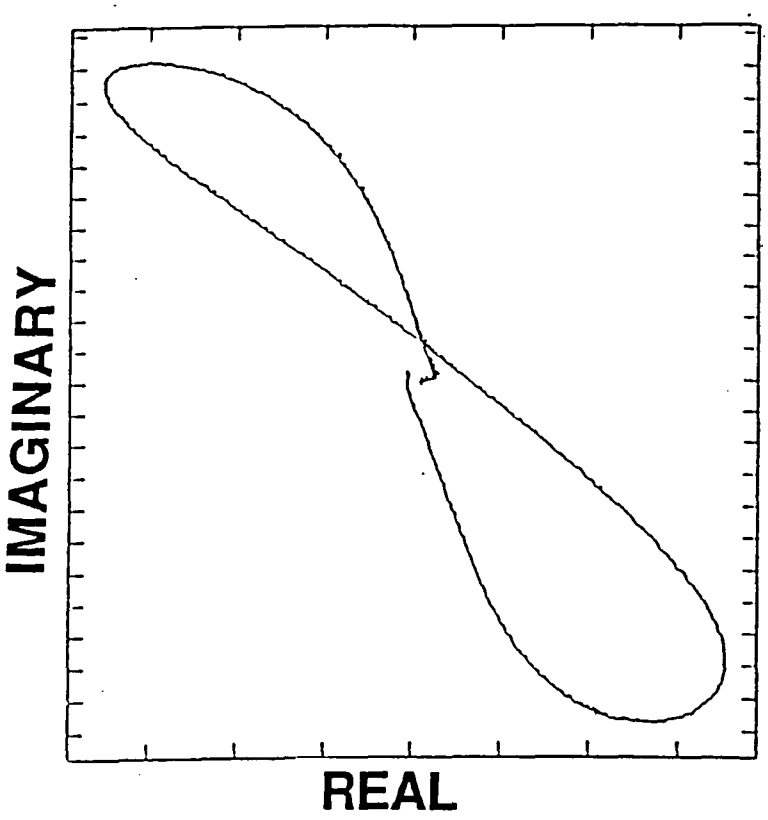

Fig. 7.8 Incomplete penetration - experimental

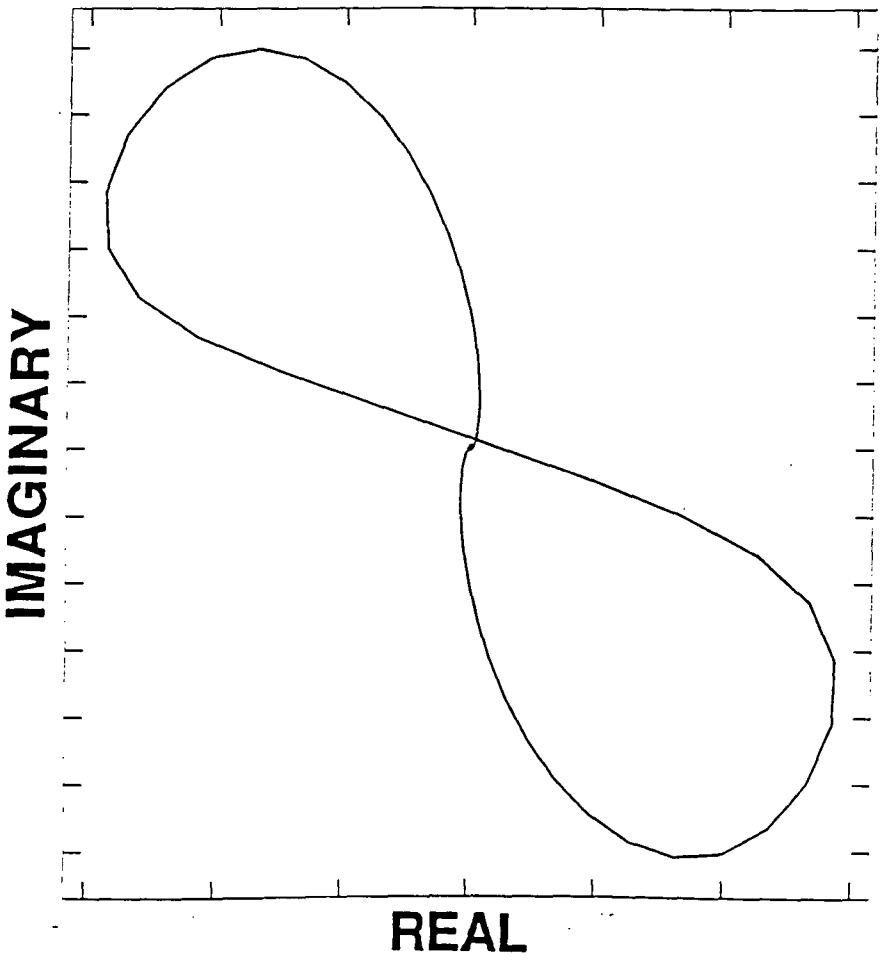

Fig. 7.9 Incomplete penetration - simulated

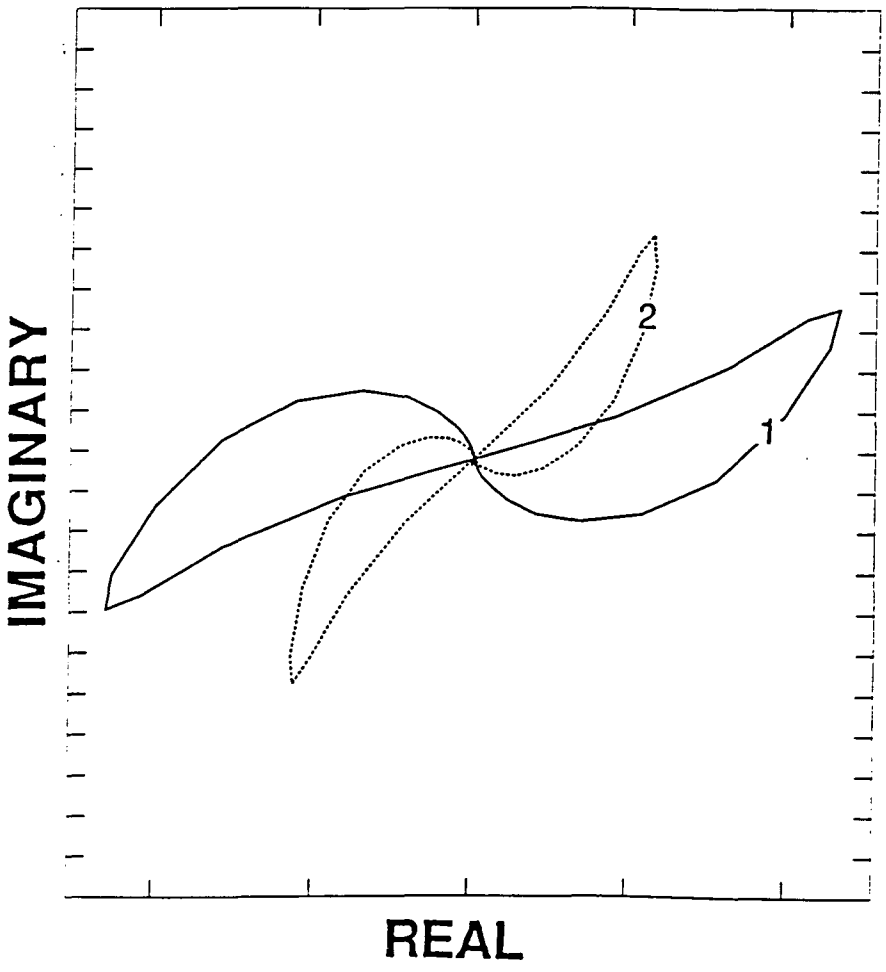

Fig. 7.10 Porosity - simulated: 1. A good weld, 2. Weld with porosity

7.6 A Unique Impedance Plane Trajectory

In practice, welds are often made between two materials of different conductivities. Often the conductivity of a specific material could vary by as much as three percent from the standard conductivity. Under these conditions the impedance plane trajectories obtained have a unique single lobed shape. Experimental results from welds between tubes of the same material produced in different batches are shown in Fig. 7.11. The single lobed IPT is a result of the differences in conductivity on either side of the weld. Usually, when the differential probe is symmetric on either side of the defect, the probe is balanced as explained in Chapter 3. However, in this case, because of the difference in conductivity on either side, the balance does not occur until the probe is clear off the weld, the heat affected regions, and entirely under the second tube. This explanation is also validated by the results shown in Fig. 7.12. The two IPT's in Fig. 7.12 were obtained from the same weld by moving the probe in opposite directions. That is, when the probe goes from say, a region of higher conductivity to a region of lower conductivity the IPT traced will be in a direction opposite to the IPT traced when the probe goes from a region of lower conductivity to a region of higher conductivity. These results are further verified by the IPT's obtained from numerical simulations shown in Fig. 7.13. A comparison of the experimental and numerical results show that with decreasing depth of penetration of the weld, the circumference of the IPT lobes increase as shown in Fig. 7.14 and Fig. 7.15. This means that defective welds could be detected based on the impedance plane trajectory

shape in these situations. Also, a single lobed IPT makes a weld signal immediately discernible from other defect signals.

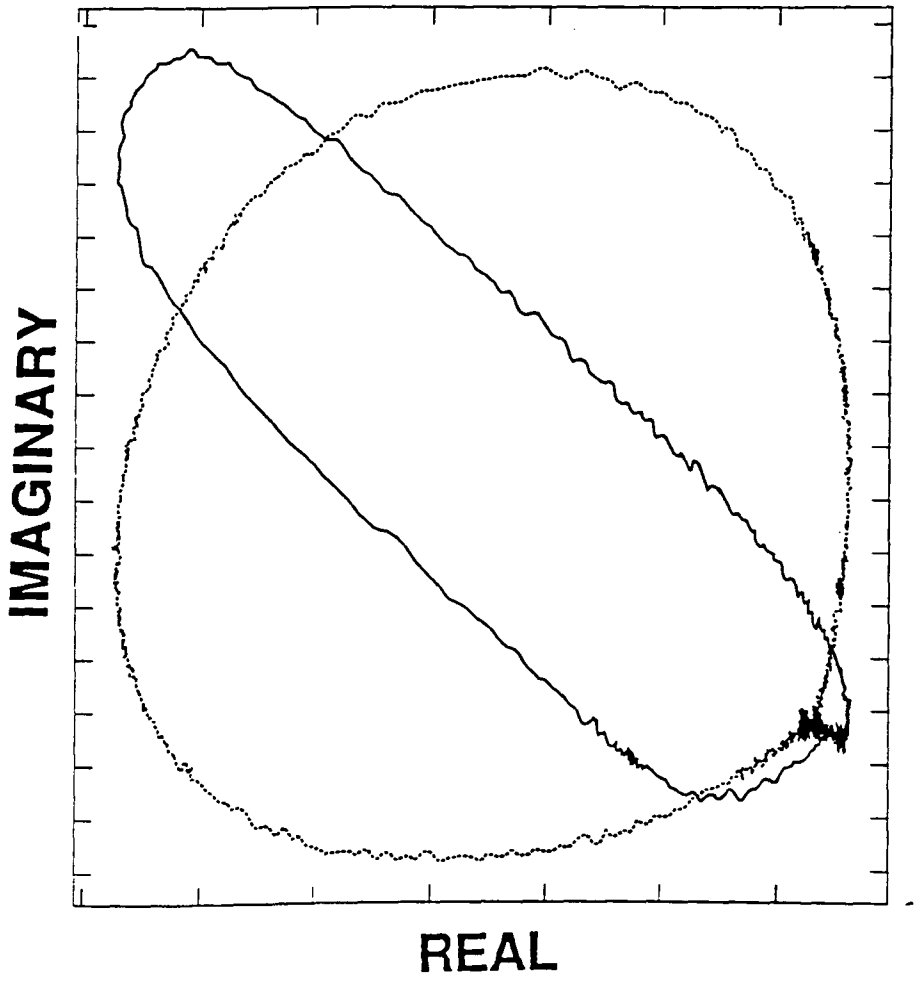

Fig. 7.11 Representative single lobed impedance plane trajectories

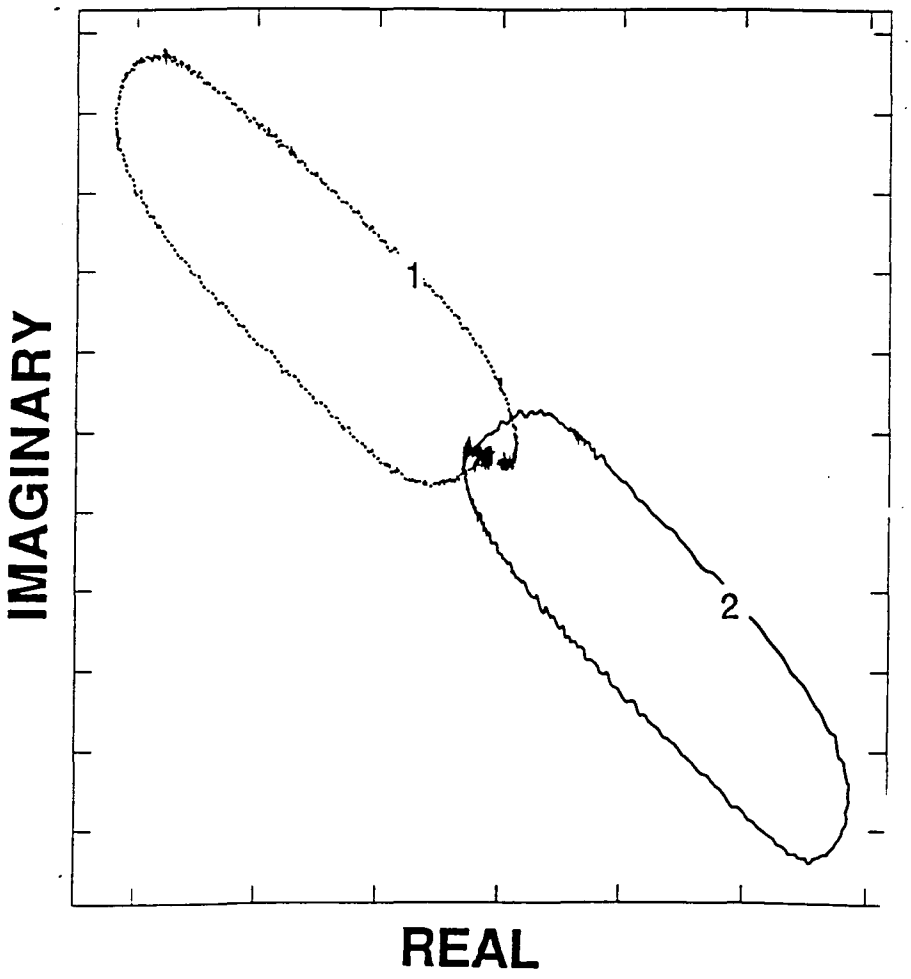

Fig. 7.12 Conductivity considerations - experimental (1 & 2 are signals from the same weld with the probe moving in opposite directions)

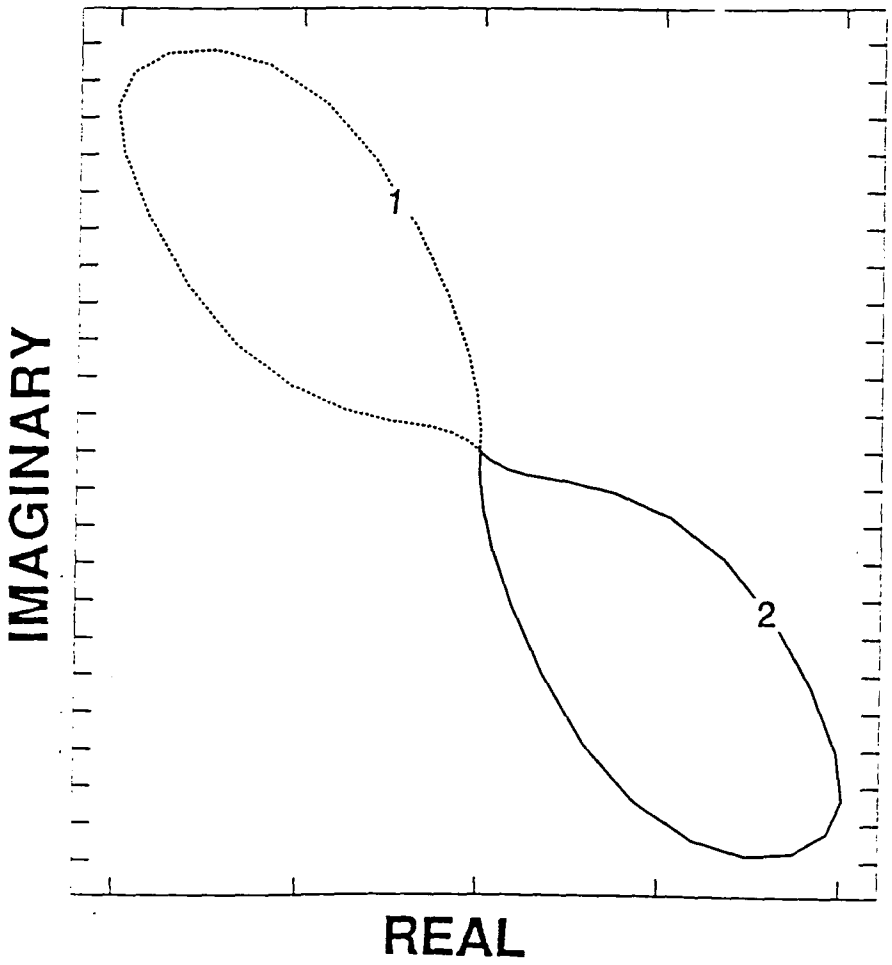

Fig. 7.13 Conductivity considerations - simulated (1 & 2 are signals from the same weld with the probe moving in opposite directions)

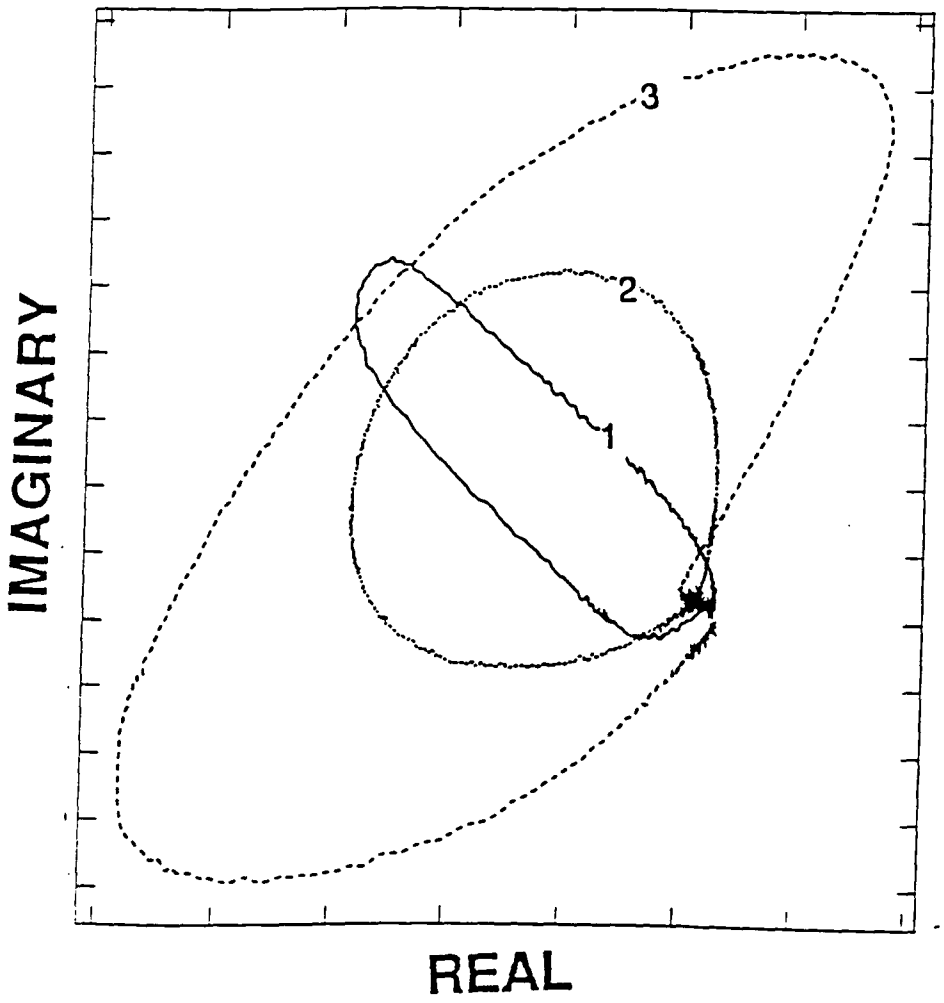

Fig. 7.14 Incomplete penetration (single lobed case) - experimental
(numbered in order of increasing incomplete penetration)

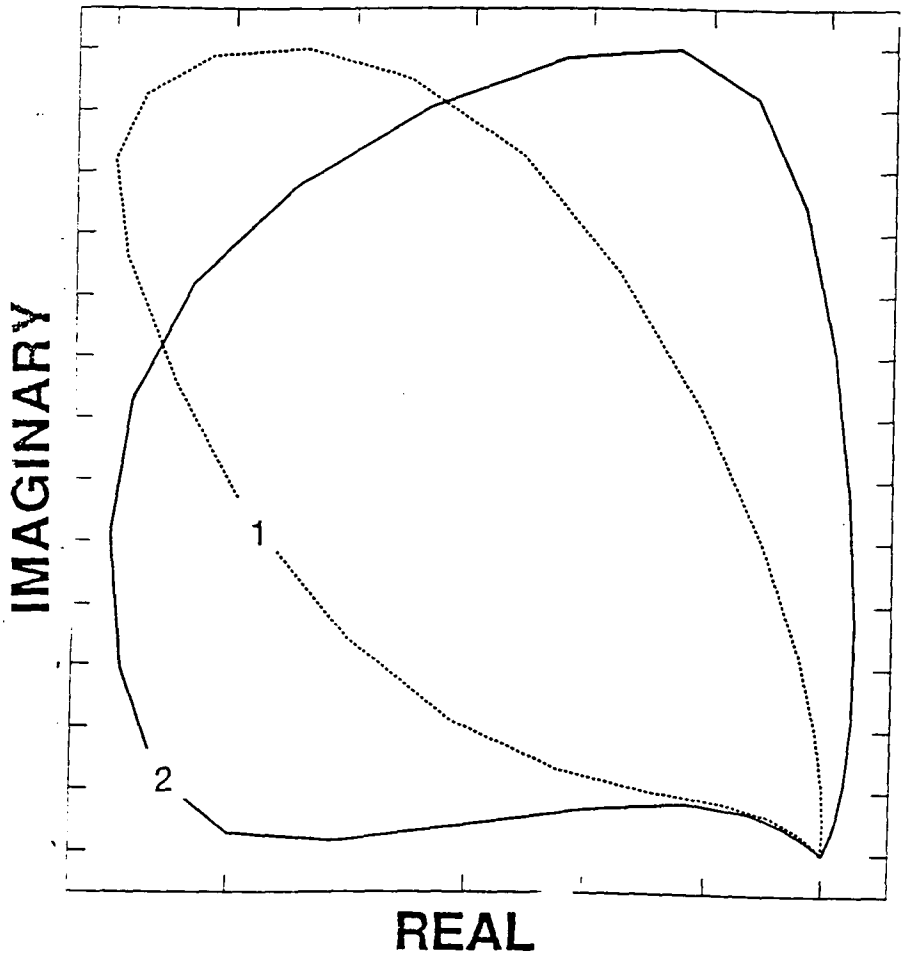

Fig. 7.15 Incomplete penetration (single lobe case) - simulated (numbered in order of increasing incomplete penetration dimension)

7.7 Classification

In an automated process it is important that signals from different sources be classified using some reliable classification technique. For a preliminary study the Fourier descriptors in conjunction with the multilayer perceptron were used to classify three classes of signals: welds, cracks and support plates. Eight sets of training data from each class were used to train the net with the back-propagation algorithm. 100% classification results were obtained using four test data sets from each of the classes. Also, a study was conducted to evaluate the Fourier descriptor data and the method of invariant moments [28]. It was found that the invariant moments had better inter-class separability to intra-class separability ratio. However, high precision calculations are required in the invariant moments technique and also reconstruction of the original signal from the invariant moments is difficult compared to the Fourier descriptors. Fig. 7.16 shows a typical output of a heat exchanger tubing defect classification using the software developed for this project. Fig. 7.16 is a classification of a weld signal actually obtained from the heat exchanger tubing. It should be noted that the impedance plane trajectory has a single lobed shape as predicted earlier. This is an extremely good indication of the validity of the experimental and numerical studies conducted in this research since the shape of the impedance plane trajectory from the heat exchanger tubing was predicted theoretically before any tests were done on the actual heat exchanger tubing.

Once the weld is classified, further analysis of the signal to locate the presence of any defects could be done using the same neural network approach or using simple phase/amplitude discrimination.

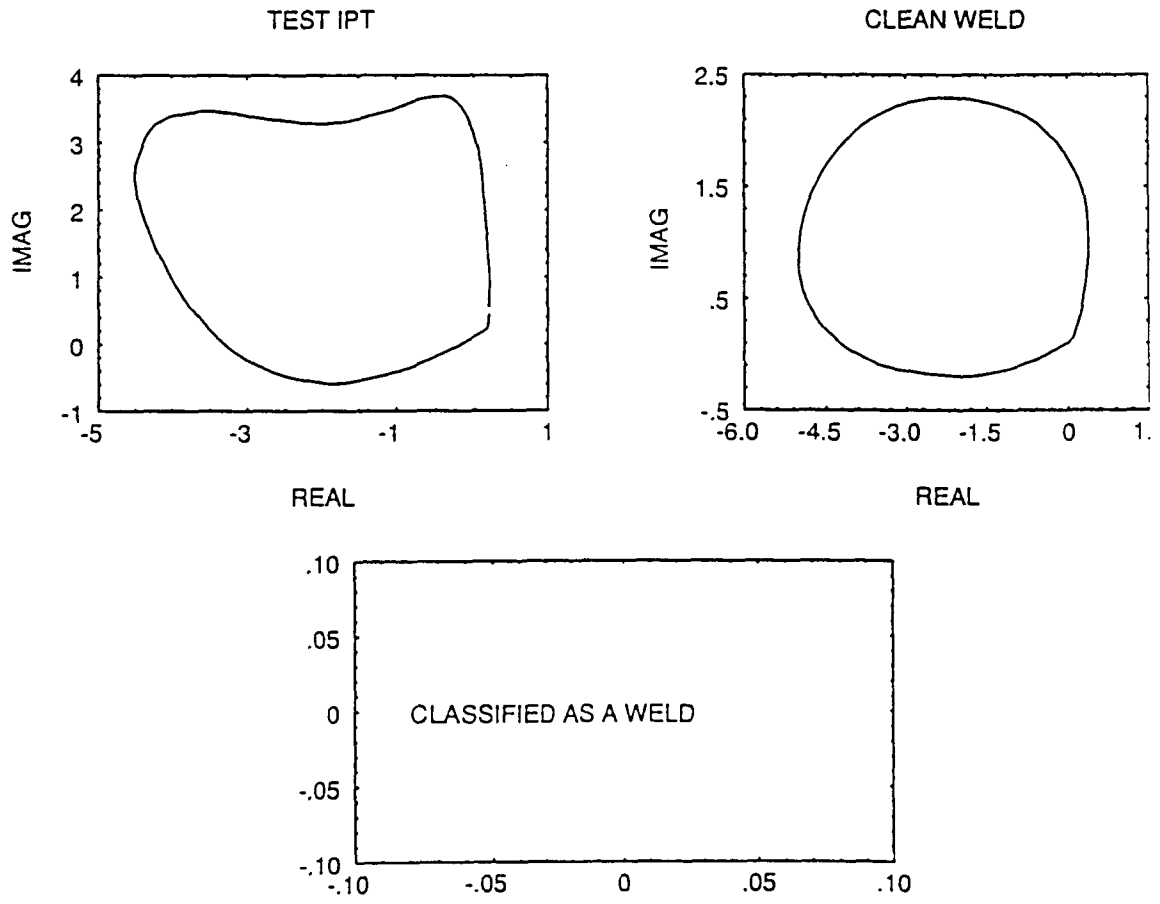

Fig. 7.16 Classification of a heat exchanger tubing weld

8 CONCLUSIONS AND FUTURE WORK

8.1 Conclusions

As indicated in Chapter 1 the objectives of this study were to determine the feasibility of using the eddy current technique in weld inspection. This study specifically targeted the inspection of the heat exchanger tubing of the space shuttle main engine.

Results obtained indicate that it is possible to detect and size different weld defects in small diameter tubing using the eddy current method and the finite element simulations. The eddy current method is quite sensitive to outer diameter cracks of small dimensions depending on the frequency of operation. The other two important methods used in weld inspection, the ultrasonic method and the radiographic method, have also given good results in terms of defect detection [14]. However, the equipment required in both cases is expensive and comparatively bulky. In the heat exchanger tubing, use of ultrasonic inspection is very difficult since the tube geometries being studied make it difficult to design an ultrasonic transducer capable of accessing the whole length of the tubing. As shown in this thesis the differential probe eddy current technique provides a safe, economical and reliable alternative to the more popular methods of radiography and ultrasonics for weld inspection.

As in other areas of inspection, for accurate detection and sizing of weld defects it is advisable to use more than one method of inspection. W.C. Harmon describes how the Farrowtest (Chapter 3.) and Ultramat [14] (an

ultrasonic technique for the automatic production testing of welds in electric resistance welded steel pipe) differ in their capability of detecting weld defects and advocates the use of both the tests for improving reliability and accuracy: ' **In detection of minor imperfections - those numerous marginal variables which are in most cases, inconsequential and not cause for rejection - the two tests differ somewhat. The Ultramat is more sensitive to long shallow ridges and grooves. The Farrowtest is much more sensitive to superficial surface defects such as small scabs. These differences constitute some justification for use of both the tests. Even though either test will detect all major defects that warrant rejection of the pipe, detection of marginal imperfections warns the operator of changing condition which, if not arrested, could lead to serious rejectable defects. Another reason for using both tests is the double assurance of detection of defects'.** It would not be possible to use either of the above techniques in the inspection of the heat exchanger tubing because of the helical windings of the heat exchanger tubing. The differential probe as discussed earlier is an easy and reliable way of inspecting curved tubing. However, weld inspection using the differential probe eddy current technique would be more reliable in detecting minor imperfections in conjunction with some other reliable weld test.

The finite element technique as shown from the results is a handy tool for understanding the physical characteristics of the weld and also to obtain sizing information of any defects. Also, signals from defects difficult to machine can very easily be simulated using the model. In effect

numerical modeling has once again been proved to be indispensable in material studies.

8.2 Future Work

One important area in which interesting research is possible in eddy current inspection of weld defects is in the suppression of the signal from good welds. In the case of heat exchanger tubing inspection the signals from good welds could be ignored without further processing and classification. Also, defect signals could easily be detected. This could be done using the multi-frequency approach [12,29] wherein unwanted signals due to the different variabilties could be suppressed by using a combination of n+1 measurements to suppress n signals. For example, to suppress lift-off variations and permeability variations, three measurements, which could be the amplitude and phase measurements at one frequency and either amplitude or phase measurement at another frequency, could be used [30]. Another method could be to use the affine transformations [31] to subtract the good-weld signal from the total signal.

More research is warranted in the eddy current inspection of ferromagnetic tubing. Also, alternative methods should be investigated for the case of thick walled tubing, where the skin depth considerations make the use of conventional eddy current testing impractical. An extension of this study with more experimental samples, and defects machined using sophisticated machinery, would throw more light on the full scale of the potential of the differential probe eddy current technique.

REFERENCES

[1] Satish, S.R., "Parametric Signal Processing for Eddy Current NDT," Ph.D. Dissertation, Colorado State University, Fort Collins, 1983.

[2] Quong, H., "SSME Heat Exchanger Coil Weld Nondestructive Inspection Review," BC 87-32, NASA Langley, 1987.

[3] Ross, G.S., "Experimental and Numerical Studies of Tight Crack Defects in Tubing," Masters Thesis, Iowa State University, Ames, 1992.

[4] Lord, W., "Prototype Eddy Current SSME Heat Exchanger Tubing Inspection System," NASA Interim Report, October, 1990.

[5] Burgess, N.T., Quality Assurance of Welded Construction, Elsevier Science Publishers Ltd., New York, 1989.

[6] Palanisamy, R., "Finite Element Eddy Current NDT Model," Ph.D. Dissertation, Colorado State University, Fort Collins, 1980.

[7] Nath, S.N., "Remote Field Eddy Current Phenomena,", M.S. Thesis, Colorado State University, Fort Collins, 1988.

[8] Erdelyi, E.A., "Nonlinear Magnetic Field Analysis of DC Machines," IEEE Transactions on Power Apparatus and Systems, Vol. PAS-89, 1970, p. 1546.

[9] Lord, W., "Numerical Modeling of Electromagnetic NDT Phenomena," New Procedures in Nondestructive Testing (Proceedings), Editor P. Holler, Springer-Verlag, Heidelberg, 1983.

[10] Lord, W., "Applications of Numerical Field Modeling To Electromagnetic Methods of Nondestructive Testing," IEEE Transactions on Magnetics, Vol. MAG-19, No. 6, November, 1983, p. 2437.

[11] Chrishlom, J., Introducing the EMD MK 3 - a New Dimension in NDT, Offshore Oil International, October, 1981.

[12] Holler, P. Becker, R. and Sharpe R.S., "The Application of Eddy Currents in Weld Testing," Welding in the World, 1984, p. 22.

[13] Harmon, W.C., "Automatic Production Testing of Electric Resistance Welded Steel Pipe," Materials Evaluation, March, 1966, p. 136.

[14] Nerwin, N.H., "Eddy Current Testing of Tubular Steel Products," Materials Evaluation, April, 1966, p. 192.

[15] Winslow, A.M., "Numerical Solution of the Quasilinear Poisson Equation in a Nonuniform Triangular Mesh," Journal of Computational Physics, Vol. 2, 1967, p. 149.

[16] Ames, W.F., Numerical Methods for Partial Differential Equations, Barnes & Noble, Inc., N.Y., 1976.

[17] Palanisamy, R. and Lord, W. "Finite Element Analysis of Eddy Current Phenomena," Materials Evaluation, Vol. 38, 1980, p. 39-43.

[18] Lord, W. and Palanisamy, R., "Finite Element Modeling of Electromagnetic NDT Phenomena," IEEE Transactions On Magnetics, Vol. MAG-15, No. 6, November 1979.

[19] Lord, W. and Palanisamy, R., "Development of Theoretical Models for NDT Eddy Current Phenomena," Eddy Current Characterization of Materials and Structure, opsit, 1981, p. 5.

[20] Bickford, W.B., A First Course in the Finite Element Method, Irwin, Homewood, 1990.

[21] Chari, M.V.K and Silvester, P., "Finite Element Solution of the Eddy Current Problem in Magnetic Structures," IEEE Transactions on Power Apparatus and Systems, Vol. PAS-93, No. 1, January-February, 1974, p. 62.

[22] Brauer, J. R., "Finite Element Analysis of Electromagnetic Induction In Transformers," Presented at the IEEE Winter Power Meeting, New York, 1977.

[23] Hu, M.K., "Visual Pattern Recognition by Moment Invariants," IRE Transactions on Information Theory,Vol. IT-8, 1962, p. 179.

[24] Granlund, G.H., "Fourier Preprocessing for Hand Print Character Recognition," IEEE Transactions on Computers, Vol. C- 21, February, 1972, p. 195.

[25] Gonzalez, R.C. and Wintz, P., Digital Image Processing, Addison-Wesley Publishing Company, Menlo Park, 1987.

[26] Lippman, R.P., "An Introduction to Computing with Neural Nets," IEEE ASSP Magazine, April, 1987, p. 4.

[27] Horwitz, P.E.H., Welding Principles and Practice, Houghton Mifflin Company, Boston, 1979.

[28] Katragadda, G., "Feature Extraction in Eddy Current Nondestructive Evaluation," Project Report, Iowa State University, 1991.

[29] Gilstad, J. Dersch, M.F. and DeNale, R., "Multifrequency Eddy Current Testing of Ferromagnetic Welds," Review of Progress in Quantitative NDE, Vol. 9, 1990, p. 1363.

[30] Libby, H., Introduction to Electromagnetic Nondestructive Test Methods, Krieger Publishing Co., New York, 1979.

[31] Stolte, J. Udpa, L and Lord, W., "Multifrequency Eddy Current Testing of Steam Generator Tubes Using Optimal Affine Transformation," Review of Progress in Quantitative NDE, Vol. 7, 1988, p. 821.

[32] Bell, E.T., Men of Mathematics, Simon and Schuster, New York, 1965

[33] Stucky, P., "Skin Depth Considerations in Eddy Current NDT,", M.S. Thesis, Iowa State University, Ames, 1991.